Check for updates

*Earthquake Engineering & Structural Dynamics*

WILEY

RESEARCH ARTICLE OPEN ACCESS

# Next-Generation Seismic Performance Assessment Through Multi-Component Ground Motion Compatible Intensifying Artificial Acceleration

M. Amin Hariri-Ardebili[1,2] | Giacomo Sevieri[3] | Carlo Resta[4] | Golsa Mahdavi[5] | Anna De Falco[4] | Siamak Sattar[1] | Sissy Nikolaou[1]

[1]National Institute of Standards and Technology (NIST), Gaithersburg, Maryland, USA | [2]University of Maryland, College Park, Maryland, USA | [3]Aon Reinsurance solutions, Milan, Italy | [4]University of Pisa, Pisa, Italy | [5]AECOM, Colorado, Denver, USA

**Correspondence:** M. Amin Hariri-Ardebili (hariri@umd.edu)

**Received:** 21 January 2026 | **Revised:** 24 August 2026 | **Accepted:** 31 August 2026

**Keywords:** artificial acceleration | dams | IDA | seismic response | soil-structure interaction

## ABSTRACT

Despite the crucial need for fully quantitative risk assessment of large-scale structures, their performance is typically assessed through deterministic or semi-quantitative approaches. The main preventing factor is the computational burden of probabilistic seismic analyses. This paper proposes a fast and accurate method that combines the capabilities of Incremental Dynamic Analysis (IDA) and endurance time methods. The method is based on intensifying artificial acceleration (IAA), which is generated based on meta-features such as spectral ordinates, nonlinear response, and hysteretic energy present in real ground motion. The IAA aims to estimate the incremental response of the structure, similar to the IDA method, but using only a single simulation. The proposed IAA method is applied to a benchmark dam and is compared to single-record IDA for various types of foundation-structure interaction assumptions, as well as for linear and nonlinear systems. Differences between multicomponent IAA and IDA in terms of drift and damage index are quantified using ten similarity and distance metrics. The findings demonstrate promising compatibility between IAA and IDA, while the former reduces computational time by up to 90%.

## 1 | Introduction

Concrete dams hold a central role in ensuring the supply of energy and water. Their strategic significance in supporting communities becomes even more pronounced during a time marked by human-induced energy crises and the escalating impact of climate change, leading to heightened occurrences of extreme events such as severe floods or prolonged dry seasons. Safeguarding these structures against natural hazards is paramount. Although concrete dams have a rich history in seismic design [1], a dependable evaluation of their seismic performance remains a crucial stride toward a more accurate assessment of their inherent natural risk [2].

The seismic assessment of concrete dams presents a formidable challenge in the realm of structural engineering due to the complex interaction among soil, structure, and basin dynamics [3]. Notably influential in this context is the role of uncertainties, stemming from the variability inherent in both materials and ground motion characteristics [4]. While incorporating uncertainty into the seismic assessment of dams is pivotal, this endeavor often imposes a substantial computational demand, which may pose challenges, especially for practitioners. This predicament is a shared concern across complex engineering systems, extending beyond concrete dams. As a response, numerous computational methodologies have emerged to address the seismic evaluation of structures. These approaches can be categorized

This is an open access article under the terms of the Creative Commons Attribution License, which permits use, distribution and reproduction in any medium, provided the original work is properly cited.

© 2026 The Author(s). *Earthquake Engineering & Structural Dynamics* published by John Wiley & Sons Ltd. This article has been contributed to by U.S. Government employees and their work is in the public domain in the USA.

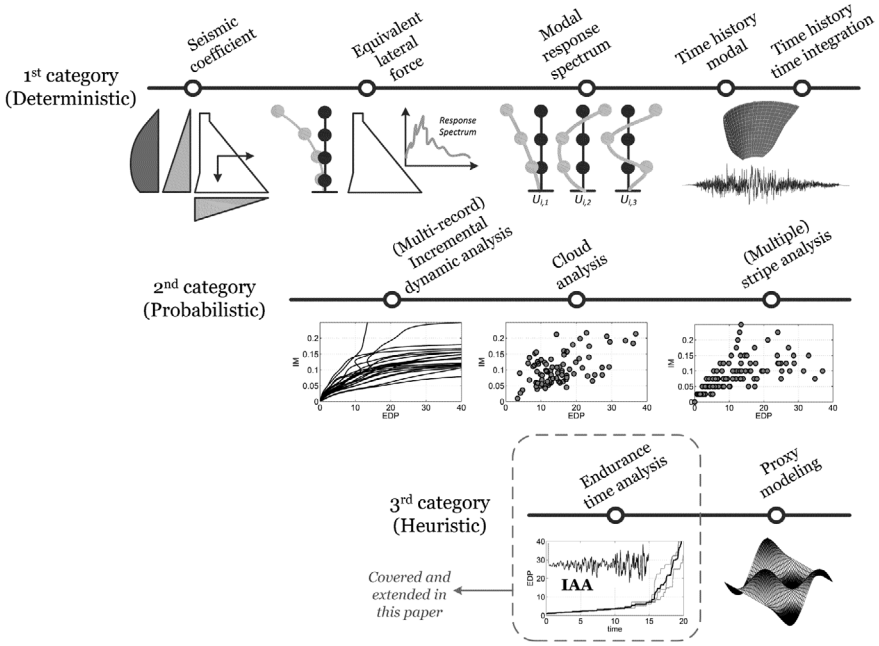



**FIGURE 1** | Historic progress of seismic performance evaluation methods in structures using a concrete dam example.

based on their treatment of uncertainties and their methods for managing computational demands. Broadly, three primary categories are discernible: (1) deterministic methods, which endeavor to analyze a single structural system through varying degrees of complexity; (2) probabilistic methods, wherein uncertainties are explicitly modeled; and (3) heuristic methods, which entail the integration of deterministic and/or probabilistic techniques with advanced statistical, optimization, or machine learning strategies to enhance the efficiency of analyses. While the classification depicted here (Figure 1) encapsulates the principal trends in dam and structural engineering, it is worth noting that these categories have fuzzy edges, and methodologies can transition between categories by altering the approach to uncertainty modeling. Subsequent to this introduction, each category is succinctly discussed.

Deterministic methodologies for the seismic assessment of dams, and by extension, complex structural systems, do not explicitly encompass aleatory or epistemic uncertainties. Within these approaches, material properties and seismic loads are treated as fixed, deterministic values. However, they can be selected to target specific reliability scenarios. For instance, this can be achieved by utilizing characteristic values for material properties and assigning a particular return period to ground motions. The categorization of these approaches can be broadly outlined as follows [5]:

**Seismic coefficient method** that is employed to appraise the seismic stability of structures [6, 7]. Seismic actions are translated into corresponding static forces, which are then combined with static loads.

**Equivalent lateral force method** operates on the assumption that a structure under seismic motion adopts a deformed shape aligned with its first natural mode. A "static correction method" can be applied to consider the higher modes [8, 9]. The total structural response is computed by combining the first mode shape load ($Q_1$), higher mode shapes load ($Q_h$), and the pre-earthquake loads ($Q_{\text{pre}}$), as $Q_{\max} = Q_{\text{pre}} \pm \sqrt{Q_1^2 + Q_h^2}$.

**Modal response spectrum analysis method** involves considering a sufficient number of modes such that at least 90% of the total mass of the system is encompassed [10].

**Modal time history analysis method** is a linear approach involves computing the solution to the dynamic equilibrium equation for structural behavior in terms of physical quantities, such as displacement and stress, that vary over time [10].

**Time history-time integration procedure** directly integrates the equations of motion in the time domain using explicit or implicit time integration techniques. This facilitates the solution of both linear and nonlinear problems [11], with resulting physical quantities varying over time.

Probabilistic methodologies explicitly account for the impact of aleatory and epistemic uncertainties in the seismic assessment of concrete dams. Several established time history analysis-based probabilistic techniques are reviewed below. It's worth noting that probabilistic approaches extend beyond time history analysis, as they have also been applied to other methods previously discussed as deterministic.

**Multi-record incremental dynamic analysis (MR-IDA)** entails conducting a series of IDAs with diverse ground motions, thereby eliminating reliance on a single seismic input's characteristics [12]. In each IDA, a reference ground motion record is scaled with respect to a specific Intensity Measure (IM) to represent Engineering Demand Parameter (EDP) at varying levels of excitation. Its computational cost can become impractical, especially for practitioners, when applied to



10969845, 0, Downloaded from https://onlinelibrary.wiley.com/doi/10.1002/eqe.70292 by National Institute Of Stds and Technology, Wiley Online Library on [02/11/2026]. See the Terms and Conditions (https://onlinelibrary.wiley.com/terms-and-conditions) on Wiley Online Library for rules of use; OA articles are governed by the applicable Creative Commons License

complex systems like concrete dams. Nevertheless, MR-IDA is widely adopted within the dam engineering scientific community [13–17].

**Cloud analysis method** seeks to establish a statistical correlation between ground motions and structural behavior by utilizing a large set of unscaled ground motion records. The outcomes are then used to calibrate a "probabilistic seismic demand model" [18] that relates IMs and EDPs in the form of a power-law equation, i.e., $EDP = a\ IM^b$, where $a$ and $b$ represent regression coefficients. The cloud analysis requires fewer dynamic simulations than IDA, yet it remains computationally demanding.

**Stripe analysis method** involves a series of specific seismic intensity levels referred to as "stripes," which are of interest to the analyst. All selected ground motions within a stripe are scaled to target a specific response spectrum. Unlike IDA, stripe analysis employs different ground motions at distinct seismic intensity levels. Consequently, it doesn't generate continuous capacity curves akin to those produced by IDA. The utilization of this method in concrete dam analysis is relatively limited [19, 20].

The final category discussed here encompasses heuristic approaches for the seismic assessment of structures. These methods draw inspiration from optimization, advanced statistics, and machine learning concepts. The primary objective of these approaches is to alleviate the computational burden compared to direct probabilistic methods, while still maintaining a satisfactory level of accuracy. Two principal groups are explored:

**Proxy modeling**: Within this framework, machine learning (including artificial intelligence) and advanced statistical techniques, such as spectral approaches, are used to construct a proxy model of the structural system. This proxy model is then employed in conjunction with one of the aforementioned seismic assessment methods. The calibrated proxy model is used instead of the actual structural system thus significantly reducing the computational burden. The proxy model calibration necessitates fewer analyses compared to a direct full probabilistic approach [18]. Various examples, utilizing machine learning [21, 22] or general polynomial chaos expansions [17, 23], can be found in the scientific literature. As of now, these methods primarily find use in research, as the definition and calibration of proxy models demand advanced technical expertise that is not commonly available beyond the scientific community. However, advancements in this field, coupled with successful instances within the scientific community, are paving the way for broader adoption among practitioners.

**Endurance time analysis (ETA)** is a time history-time integration technique that uses an endurance time excitation function (ETEF) to estimate the seismic behavior of a structure under escalating excitation levels. Conceptually, it resembles a dynamic pushover procedure [24], aiming to subject the structure to a range of seismic intensities from low to high. During this process, structural responses are recorded across linear and non-linear regimes, all in a single simulation [25]. ETA also has the capacity to capture structural failure at higher intensity levels. In essence, the longer a structure can endure the applied endurance time excitation before failure, the stronger the structure is [26]. The key distinction between ETA and other probabilistic methods, such as IDA, lies in ETA's requirement for fewer dynamic simulations. Although ETA employs a time history-time integration scheme to solve the finite element model, it does not rely on a specific ground motion record, either real or synthetic. Consequently, the results of the numerical simulation need suitable post-processing to be applicable in engineering practice. Hence, ETA is classified among heuristic approaches. Numerous studies have explored ETA's application in assessing the seismic performance of concrete dams, such as [27–29]. Aside from dams, ETA has also been used for the life-cycle fragility assessment of bridges [30], base-isolated structures [31], underground structures [32], and tunnels [33]. In addition, ETA has been modified to account for near-fault pulse-like ground motions [34], multiple earthquakes [35], and multi-directional seismic performance assessment [36].

In this paper, the term **intensifying artificial acceleration (IAA)** is used for the record-specific acceleration function developed to reproduce the intensity-dependent response associated with a particular ground motion record. Therefore, the IAA considered herein should be distinguished from conventional ETEF, which are generally developed based on codified, smoothed, or ensemble-average spectral targets. The derivation of a ground-motion-compatible IAA involves an optimization process, elaborated upon in the subsequent section.

It is crucial to clarify that an IAA should not be categorized as a ground motion, whether real or synthetic. Although both IAAs and ground motion records appear as acceleration time series, their intrinsic natures and purposes significantly diverge. An IAA serves as an analytical tool designed to yield outcomes analogous to those derived from a specific ground motion record. Overlooking this distinction could lead to considerable misconceptions regarding the intended application of IAA.

## 1.1 | Problem Statement and Contributions

The original ETA procedure proposed by [24] offers computational efficiency compared to other probabilistic seismic analysis methods, while providing a reasonable estimate of the median response within probabilistic frameworks [37]. Nonetheless, while IDA, cloud, and stripe analyses provide information on ground-motion record-to-record (RTR) variability, i.e., response dispersion, conventional ETA lacks this capability [38]. This limitation arises because conventional ETA are generally optimized using codified, smoothed, or ensemble-average response spectra and are intended primarily to estimate the central tendency of structural response rather than to reproduce the response associated with a particular ground-motion record. The key novelty of this paper lies in developing and validating a ground-motion-specific IAA framework against the corresponding single-record IDA. In alignment with the guidelines established by the American Society of Mechanical Engineers (ASME) [39], validation refers to establishing the degree to which a conceptual model accurately represents real-world physical phenomena for



10969845, 0, Downloaded from https://onlinelibrary.wiley.com/doi/10.1002/eqe.70292 by National Institute Of Stds and Technology, Wiley Online Library on [02/11/2026]. See the Terms and Conditions (https://onlinelibrary.wiley.com/terms-and-conditions) on Wiley Online Library for rules of use; OA articles are governed by the applicable Creative Commons License

its intended application. In the context of this paper, the proposed ground-motion-specific IAA is regarded as the "conceptual method," and its accuracy is evaluated through comparison with IDA, which involves the incremental scaling of a ground-motion record and the corresponding dynamic analyses. This comparison does not imply that IDA constitutes the definitive or exact method for assessing structural seismic response. Several studies have identified limitations associated with the use of excessively large ground-motion scale factors (SFs) [40–43]. Nevertheless, because the IAA examined in this study is developed for a specific ground-motion record, the corresponding single-record IDA provides an appropriate benchmark for evaluating its accuracy and credibility. A preliminary single-component implementation of this concept was presented by [44], who developed a record-specific IAA based on the horizontal component of a selected ground motion and examined its deconvolution and response performance. The present study extends that proof of concept to multicomponent excitation through compatible horizontal and vertical IAAs and provides a broader quantitative validation across linear and nonlinear models, massed and massless foundations, multiple IMs and EDPs, and complementary similarity, distance, stress, and damage measures.

Although the adopted optimization formulation builds upon previous developments in ETA, for which a reliable IAA is essential [45], its objective differs from that of conventional ETA. Rather than estimating only the central response associated with a generic or ensemble-based target, the proposed framework seeks to reproduce the intensity-dependent response of a particular ground-motion record. Specifically, this paper introduces an optimization process for two-component (horizontal and vertical) IAAs based on a specific target ground-motion record. This development also provides the basis for generating record-specific IAAs for a suite of ground motions, potentially allowing the corresponding set of capacity curves and their RTR dispersion to be estimated with substantially fewer non-linear dynamic analyses than multi-record IDA. The authors' contributions can be summarized as follows:

- Comparison of the dynamic response of a dam using single-record multi-component IDA and IAA methods;
- Generation of multicomponent IAAs compatible with real ground motion records;
- Deconvolution of IAAs for application in soil-structure interaction (SSI) models;
- Evaluation of method accuracy for both massed and massless foundation assumptions, linear and nonlinear concrete dam models;
- Quantification and analysis of efficient IM parameters for comparing the similarity of IDA and IAA curves.

In this initial study, we focused on comparing the proposed IAA approach using a single ground motion record to simplify and clarify the validation process. This approach allowed us to clearly analyze the IAA's response without the complexities of RTR variability, providing a clear basis for understanding its effectiveness. Focusing on a singular instance facilitated a detailed exploration of the structural mechanics aspects of the IAA method. This method sets a solid foundation for future research, which will expand to include comparisons with multiple ground motion records in a probabilistic framework. The next steps involve exploring MR-IDA and multi-record IAA (MR-IAA), aiming to quantify biases and dispersions associated with RTR variability.

The remaining sections of this paper focus on the following topics: Section "Generating Ground Motion-Compatible IAA" discusses the theory and concept of the multicomponent ground motion compatible IAA records; Section "Case Study" outlines the finite element model of the benchmark case study; and Section "Results" compares the results of IDA and IAA for various types of responses separately in horizontal and vertical directions, and also the damage profile.

## 2 | Generating Ground Motion-Compatible IAA

### 2.1 | Theoretical Formulation

Artificial intensifying accelerations are generated through an optimization process, incorporating distinct attributes specified by the analyst. Within these attributes, two fundamental traits stand out [45]: (1) the response spectra of the excitation demonstrate an approximately linear increase over time, and (2) the acceleration time history profile exhibits an increasing trend over time. While these two characteristics are frequently utilized, artificial intensifying functions can be generated to align with other parameters present in real ground motions. Notably, [46] introduced the concepts of hysteretic energy and cumulative absolute velocity [47] in the generation process.

The generation process starts from a zero-mean stationary random acceleration function, denoted here by $g(t)$. In stochastic ground-motion simulation, such a function can be generated in the time domain or through spectral representation methods [48–51]. For example, a stationary Gaussian process may be represented as

$$g(t) = \sum_{k=1}^{N_\omega} \sqrt{2G(\omega_k)\Delta\omega}\cos(\omega_k t + \phi_k), \tag{1}$$

where $G(\omega_k)$ is the target power spectral density, $\Delta\omega$ is the frequency increment, and $\phi_k$ are independent phase angles usually sampled from a uniform distribution over $[0, 2\pi]$. In the simplest implementation, $g(t)$ may be generated as band-limited white noise and subsequently shaped in the frequency domain. This initial signal should not be interpreted as a ground motion record; it only provides the initial candidate function for the optimization procedure.

The stationary signal is then converted to a nonstationary acceleration function using a deterministic modulating or envelope function,

$$Z(t) = M(t)g(t), \tag{2}$$

where $M(t)$ controls the time variation of the amplitude. Different envelope functions may be used, including piecewise linear or



10969845, 0, Downloaded from https://onlinelibrary.wiley.com/doi/10.1002/eqe.70292 by National Institute Of Stds and Technology, Wiley Online Library on [02/11/2026]. See the Terms and Conditions (https://onlinelibrary.wiley.com/terms-and-conditions) on Wiley Online Library for rules of use; OA articles are governed by the applicable Creative Commons License

trapezoidal envelopes, exponential build-up and decay functions, and Arias-intensity-based envelopes [50–52].

The non-stationary signal is then transformed into the frequency domain as

$$Z(i\omega) = \mathcal{F}\{Z(t)\}, \tag{3}$$

where $i$ is the imaginary unit, $\omega$ is the circular frequency, and $\mathcal{F}\{\cdot\}$ denotes the Fourier transform. To avoid unrealistic frequency content, the signal is filtered. A common choice is the Clough–Penzien-type filter, which combines high-pass and low-pass filtering:

$$A(i\omega) = Z(i\omega)H_1(i\omega)H_2(i\omega), \tag{4}$$

where

$$H_1(i\omega) = \frac{1 + 2i\xi_1(\omega/\omega_1)}{1 - (\omega/\omega_1)^2 + 2i\xi_1(\omega/\omega_1)},$$
$$H_2(i\omega) = \frac{(\omega/\omega_2)^2}{1 - (\omega/\omega_2)^2 + 2i\xi_2(\omega/\omega_2)}. \tag{5}$$

where $\omega_1$ and $\xi_1$ are the frequency and damping coefficients of the low-pass filter, while $\omega_2$ and $\xi_2$ are the corresponding parameters of the high-pass filter. Other filtering alternatives can also be used, including Kanai–Tajimi or Clough–Penzien power spectral density models, Butterworth band-pass filters, Ormsby-type filters, or seismological source-path-site filters that account for source spectrum, attenuation, site amplification, and high-frequency decay [51, 53–55]. The selection of the filter depends on the intended frequency range, target spectrum, and numerical stability requirements.

The filtered acceleration function is then modified so that its response spectrum approaches the target spectrum. In spectral-shaping procedures, this can be done iteratively by updating the frequency-domain amplitude according to

$$A_{\text{new}}(i\omega) = A_{\text{old}}(i\omega)\frac{S_a^*(\omega)}{S_a(\omega)}, \tag{6}$$

where $S_a^*(\omega)$ is the target acceleration response spectrum and $S_a(\omega)$ is the response spectrum of the current generated signal. Wavelet-based spectral matching may also be used for this step, where localized wavelets are added in the time domain to reduce spectral misfit while limiting undesirable changes to the non-stationary character of the signal [56].

Finally, an increasing profile is applied so that the resulting acceleration function becomes intensifying with time. This profile is commonly taken as linear,

$$l(t) = \frac{t}{t_{\text{trg}}}, \tag{7}$$

where $t_{\text{trg}}$ is the target time.

In this study, the resulting acceleration function is treated as the initial candidate $\ddot{u}_g(t)$ in the optimization process. Starting from this candidate, the optimization algorithm iteratively updates $\ddot{u}_g(t)$ to minimize the mismatch between the response quantities generated by the IAA and their corresponding target values. These artificial functions can be generated using different techniques, such as wavelet transform, evolutionary algorithms, particle swarm optimization, and increasing sine functions [57]. modified the artificial excitations by adding corrected tapered cosine wavelets in the specific time domain to match the corresponding target spectra [58]. improved the artificial excitations by adding more restrictions to their target time and presenting it as a function of both peak ground acceleration (PGA) and Arias intensity [59]. proposed a modification using a time-domain spectral matching method. This paper follows the methodology proposed by [46], which integrates acceleration spectra, nonlinear displacement, and absorbed hysteretic energy into the optimization process. However, the target quantities in this paper are derived from a particular ground motion record rather than from a design or averaged response spectrum. Therefore, the objective function computes the differences between the dynamic attributes of the candidate IAA and the corresponding target values of the selected ground motion record, as follows:

$$F_{IAA}(\ddot{u}_g) = \int_{T=0}^{T_{\max}} \int_{t=0}^{t_{\max}} \left[S_a(t,T) - S_a^*(t,T)\right]^2 \mathrm{d}t\,\mathrm{d}T$$
$$+ \int_{\mu=1}^{\mu_{\max}} \int_{T=0}^{T_{\max}} \int_{t=0}^{t_{\max}} \left\{ \begin{array}{l} \alpha_{u_m}\left[u_m(t,T,\mu) - u_m^*(t,T,\mu)\right]^2 \\ +\alpha_{E_H}\left[E_H(t,T,\mu) - E_H^*(t,T,\mu)\right]^2 \end{array} \right\} \mathrm{d}t\,\mathrm{d}T\,\mathrm{d}\mu, \tag{8}$$

where $\ddot{u}_g(t)$ is the acceleration time series of the IAA, and $S_a(t,T)$, $u_m(t,T,\mu)$, and $E_H(t,T,\mu)$ are the acceleration spectrum, nonlinear single-degree-of-freedom (SDOF)-based displacement, and hysteretic energy demand obtained from the IAA, respectively. Similarly, $S_a^*(t,T)$, $u_m^*(t,T,\mu)$, and $E_H^*(t,T,\mu)$ are the corresponding target acceleration spectrum, nonlinear bilinear SDOF-based displacement, and hysteretic energy demand imposed by the selected ground motion record. Here, $T$ and $\mu$ refer to the initial vibration period and displacement ductility ratio of the reference nonlinear bilinear SDOF system, respectively. The coefficient $\alpha$ is a weight factor that controls the relative contributions of nonlinear SDOF-based displacement and hysteretic energy to the objective function compared with the acceleration spectrum, and is defined as:

$$\alpha_{u_m}(\mu) = \frac{\mathcal{N}_{S_a}}{\mathcal{N}_{u_m}(\mu)}, \qquad \alpha_{E_H}(\mu) = \frac{\mathcal{N}_{S_a}}{\mathcal{N}_{E_H}(\mu)}. \tag{9}$$

where $\mathcal{N}_{S_a} = \int_0^{T_{\max}} \int_0^{t_{\max}} \left[S_a^*(T,t)\right]^2 \mathrm{d}t\,\mathrm{d}T$, $\mathcal{N}_{u_m}(\mu) = \int_0^{T_{\max}} \int_0^{t_{\max}} \left[u_m^*(t,T,\mu)\right]^2 \mathrm{d}t\,\mathrm{d}T$, and $\mathcal{N}_{E_H}(\mu) = \int_0^{T_{\max}} \int_0^{t_{\max}} \left[E_H^*(t,T,\mu)\right]^2 \mathrm{d}t\,\mathrm{d}T$.

The dynamic characteristics of the IAA are derived through analyses of both linear and nonlinear responses of SDOFs. These SDOFs are characterized by their periods and strength levels. The strength level or capacity is denoted by $F_y(T,\mu)$ and is a function of period and ductility ratio. $F_y(T,\mu)$ is the minimum lateral strength capacity that an SDOF system with a period of $T$ requires to avoid the average ductility ratio demands larger than $\mu$ under a particular ground motion record. The yield strength is derived using empirical relationships as outlined



10969845, 0, Downloaded from https://onlinelibrary.wiley.com/doi/10.1002/eqe.70292 by National Institute Of Stds and Technology, Wiley Online Library on [02/11/2026]. See the Terms and Conditions (https://onlinelibrary.wiley.com/terms-and-conditions) on Wiley Online Library for rules of use; OA articles are governed by the applicable Creative Commons License

by [60]. To evaluate the objective function, $t$ is discretized at $2^{11} = 2048$ points with a time increment 0.01 s; $T$ is discretized at 120 points, which are logarithmically distributed between 0.02 and 5.00 s; and $\mu$ is discretized at three points: 2, 4, and 8.

A linear profile is used in this study; therefore, $S_a^*(t,T)$ is calculated as follows:

$$S_a^*(t,T) = \frac{t}{t_{\text{trg}}} S_a^{\text{GM}}(T), \tag{10}$$

where $S_a^{\text{GM}}(T)$ represents the target acceleration spectra, that is, the acceleration spectra of a specific ground motion. $t_{\text{trg}}$ is the time at which the IAA matches the target spectrum. Although $t_{\text{trg}}$ is optional, it is fixed to be 10 s in this paper. This means that the response spectrum from the generated IAA matches reasonably the target one at $t = 10$ s.

The non-linear displacement time history is computed by analyzing reference SDOF systems with bilinear non-degrading hysteretic behavior. Therefore, the selected reference SDOF model does not explicitly capture stiffness degradation, strength deterioration, or pinching effects.

$$m\ddot{u} + c\dot{u} + f_s(u) = -m\ddot{u}_g, \tag{11}$$

where $m$ is the mass, $c$ is the viscous damping coefficient, $f_s(u)$ is the non-linear resisting force, $u$ is the relative (nonlinear) displacement with respect to ground and $\ddot{u}_g$ is the ground acceleration.

The non-linear SDOF-based displacement imposed by a particular ground motion record is computed as:

$$u_m^{\text{GM}}(T,\mu) = \max\left(|u(\tau)|\right); \quad 0 \le \tau \le t \tag{12}$$

and the target nonlinear displacement for the IAA is:

$$u_m^*(t,T,\mu) = h_{u_m}(t,T,\mu) \times u_m^{\text{GM}}(T,\mu), \tag{13}$$

where $h_{u_m}(t,T,\mu)$ is the variation function of target non-linear SDOF-based displacement in time for a particular ground motion. For a specific ground motion record, $h_{u_m}(t,T,\mu)$ is calculated by scaling the record to multiple intensity levels and computing the nonlinear displacement demand of the corresponding SDOF oscillator at each scale factor. The scale factor $\lambda$ is then mapped to the IAA time axis as $\lambda = \frac{t}{t_{\text{trg}}}$, where $t_{\text{trg}}$ is the target time. Therefore, this function specify how the target non-linear SDOF-based displacement evolve with time during the intensifying excitation, while $u_m^{GM}(T,\mu)$ defines their final target amplitudes for the selected ground motion record.

In the development of IAAs, a bilinear elasto-plastic model was utilized to define the force-displacement relationship. This model was chosen for its simplicity and broad applicability to various structural systems. While alternative nonlinear models with more detailed backbone curves exist (e.g., modified IMK), incorporating such models would significantly increase the number of design variables. This increase could render the optimization process impractical due to the expanded complexity and computational demands. Therefore, to maintain a balance between model fidelity and the feasibility of optimization, the bilinear model was deemed the most appropriate choice for this study.

In addition, the hysteretic energy in the structure with period $T$ and ductility $\mu$ is computed as:

$$E_H^{\text{GM}}(T,\mu) = \int_0^t f_s(\tau)\dot{u}(\tau)d\tau - \frac{f_s^2(t)}{2k}, \tag{14}$$

where $\dot{u}$ is the velocity response, and $k$ presents the stiffness. Subsequently, the target hysteretic energy for the IAA is:

$$E_h^*(t,T,\mu) = h_{E_h}(t,T,\mu) \times E_H^{\text{GM}}(T,\mu), \tag{15}$$

where $h_{E_h}(t,T,\mu)$ is the variation function of target hysteretic energy in time for that particular ground motion.

## 2.2 | Application and Optimization

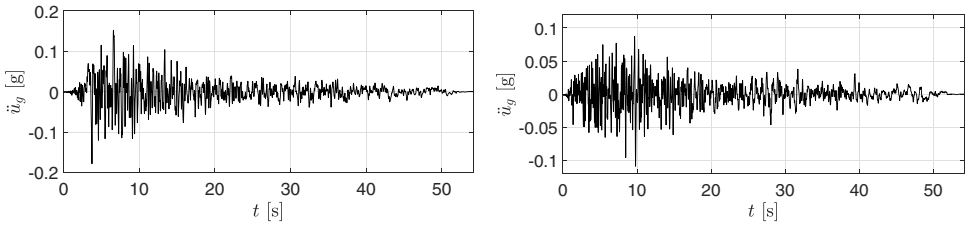
As this paper serves as a proof-of-concept study, it explores the details of only one ground motion record, and its application in comparison to the IDA method. Specifically, the Taft Lincoln School Tunnel, also known as Taft, from the Kern County, California Earthquake that occurred on July 21, 1952, serves as the focal ground motion. By adopting this approach, the case study in this paper aligns with other instances documented in the scientific literature, such as [61]. Figure 2a illustrates the horizontal and vertical components of the acceleration time-series.

Employing the procedure outlined in Section "Theoretical Formulation" produces horizontal and vertical IAA time series, as depicted in Figure 2b. These acceleration time series are complemented by their respective envelopes, referred to as zero-period acceleration (ZPA). In real ground motion records, $\text{ZPA}_H$ and $\text{ZPA}_V$ correspond to $\text{PGA}_H$ and $\text{PGA}_V$, respectively. Notably, while the IAA doesn't constitute a real ground motion record, this paper employs the term ZPA to denote the maximum absolute acceleration value attained by the IAA up to the current time $t$, that is, $\max_{\tau\in[0,t]} |\ddot{u}(\tau)|$.

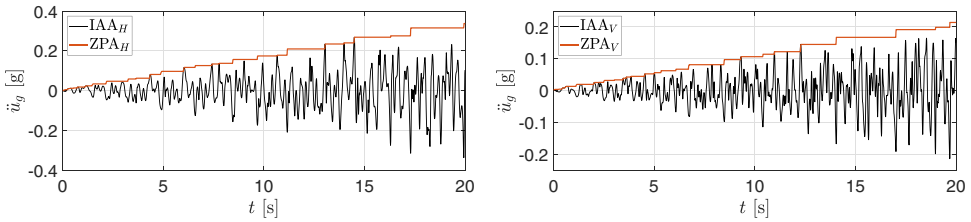
It is always beneficial to quantify the residuals of the objective function in terms of the contributing parameters, that is, spectral acceleration, non-linear SDOF-based displacement, and hysteretic energy. Such quantification aids analysts in comprehending potential discrepancies between response quantities following finite element simulations. In this context, three normalized residual models are employed, dependent on time, period, and ductility, as outlined by [46]. However, for the sake of conciseness, the ultimate values are averaged, yielding a scalar residual parameter.



10969845, 0, Downloaded from https://onlinelibrary.wiley.com/doi/10.1002/eqe.70292 by National Institute Of Sids and Technology, Wiley Online Library on [02/11/2026]. See the Terms and Conditions (https://onlinelibrary.wiley.com/terms-and-conditions) on Wiley Online Library for rules of use; OA articles are governed by the applicable Creative Commons License




(a) Real ground motion; left: horizontal component; right: vertical component




(b) Intensifying artificial acceleration; left: horizontal component; right: vertical component

**FIGURE 2** | Characteristics of the target ground motion record (i.e., Taft record), and the corresponding IAA.

$$\begin{cases} \mathrm{Res}_{S_a}^{\mathrm{norm}} = \dfrac{1}{(T_{\max}-T_{\min})}\displaystyle\int_{T_{\min}}^{T_{\max}} \frac{\int_0^{t_{\max}} [S_a(t,T)-S_a^*(t,T)]\,\mathrm{d}t}{\int_0^{t_{\max}} S_a^*(t,T)\mathrm{d}t}\mathrm{d}T \\ \mathrm{Res}_{u_m}^{\mathrm{norm}} = \dfrac{1}{(T_{\max}-T_{\min})(\mu_{\max}-1)}\displaystyle\int_1^{\mu_{\max}}\int_{T_{\min}}^{T_{\max}} \frac{\int_0^{t_{\max}} [u_m(t,T,\mu)-u_m^*(t,T,\mu)]\,\mathrm{d}t}{\int_0^{t_{\max}} u_m^*(t,T,\mu)\mathrm{d}t}\mathrm{d}T\mathrm{d}\mu \\ \mathrm{Res}_{E_H}^{\mathrm{norm}} = \dfrac{1}{(T_{\max}-T_{\min})(\mu_{\max}-1)}\displaystyle\int_1^{\mu_{\max}}\int_{T_{\min}}^{T_{\max}} \frac{\int_0^{t_{\max}} \left[E_H(t,T,\mu)-E_H^*(t,T,\mu)\right]\,\mathrm{d}t}{\int_0^{t_{\max}} E_H^*(t,T,\mu)\mathrm{d}t}\mathrm{d}T\mathrm{d}\mu. \end{cases} \tag{16}$$

The continuous objective function in Equation (8) is evaluated in discrete form by sampling time, period, and ductility ratio as $t_j$, $T_i$, and $\mu_k$, respectively. In the present implementation, the optimization variables are the wavelet coefficients used to represent the candidate IAA acceleration time history $\ddot{u}_g(t)$. After each iteration, the candidate IAA is reconstructed in the time domain and the corresponding $S_a(t,T)$, $u_m(t,T,\mu)$, and $E_H(t,T,\mu)$ values are recomputed. The optimization is performed using a nonlinear unconstrained trust-region reflective algorithm [62]. The iterative process is continued until the reduction in the objective function, or equivalently the reduction in the normalized residuals, becomes smaller than a prescribed tolerance, or until the maximum number of iterations is reached.

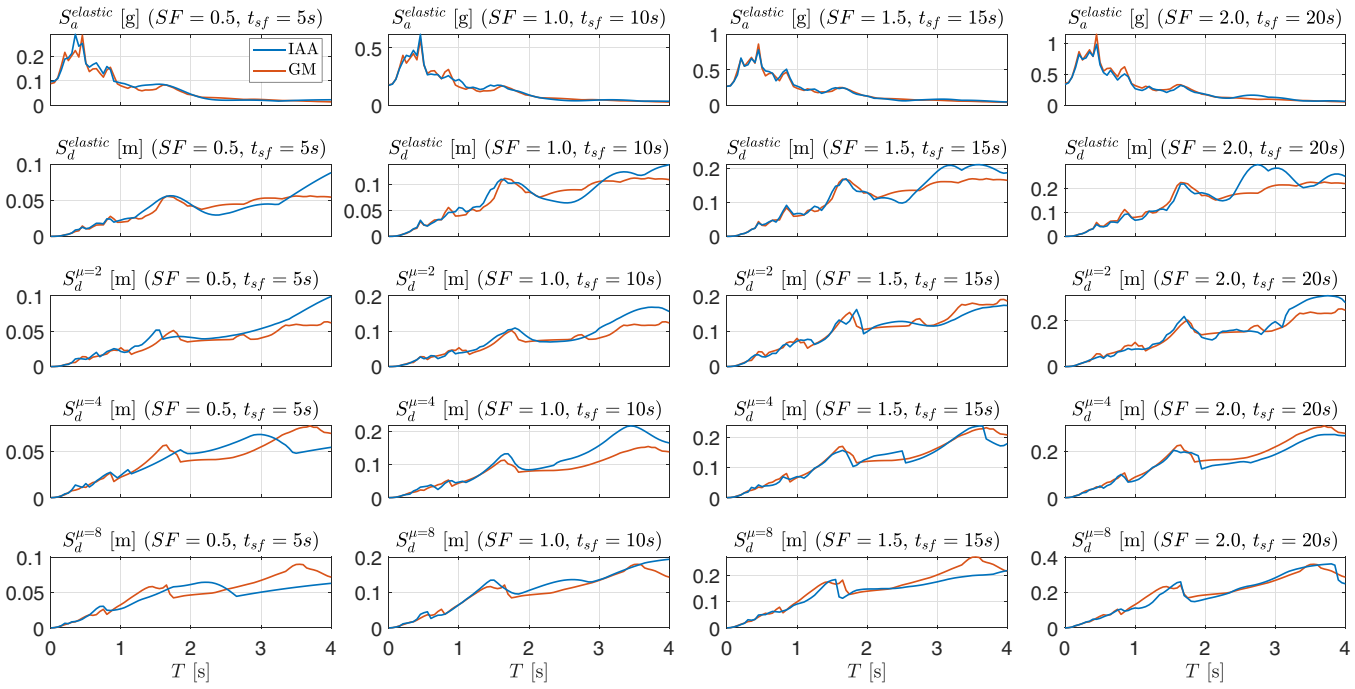
The computed normalized residuals for the horizontal component of Taft record are: $\mathrm{Res}_{S_a}^{\mathrm{norm}} = 8\%$, $\mathrm{Res}_{u_m}^{\mathrm{norm}} = 16\%$, and $\mathrm{Res}_{E_H}^{\mathrm{norm}} = 14\%$. For the vertical component the residuals are higher: $\mathrm{Res}_{S_a}^{\mathrm{norm}} = 16\%$, $\mathrm{Res}_{u_m}^{\mathrm{norm}} = 20\%$, and $\mathrm{Res}_{E_H}^{\mathrm{norm}} = 22\%$. While these values may seem high, the optimized IAAs should be acceptable for practical purposes. In addition, the true challenge is to compare the results of IAA and IDA for the case study (which is discussed in Section Results).

Figure 3 presents a comparison between the response spectra of the real ground motion and the generated IAA for the horizontal component. Figure 3 compares the response spectra, and Figure 3 presents the hysteretic energy and non-linear SDOF-based displacement terms. It's important to note that a similar plot is available in the Appendix, Figure A1, which corresponds to the vertical component. The response spectra are illustrated through both the elastic acceleration spectrum and inelastic displacement spectra, encompassing four distinct ductility ratios: 1 (equivalent to the elastic spectrum), 2, 4, and 8. Notably, the chosen ground motion record showcases a fluctuating acceleration spectrum within short periods, spanning from 0.2 to 0.4 s, thereby introducing complexity to the IAA optimization process. As observed previously, the optimization process fares better for the horizontal component compared to the vertical counterpart. Additionally, the alignment in acceleration spectra is more pronounced than that in nonlinear displacement spectra. These comparisons are depicted for four scale factors of the real ground motion, that is, SF = 0.5, 1.0, 1.5, and 2.0, alongside their corresponding IAA responses evaluated at the mapping times $t_{\mathrm{sf}} = 5, 10, 15$, and 20 s, respectively.[1]

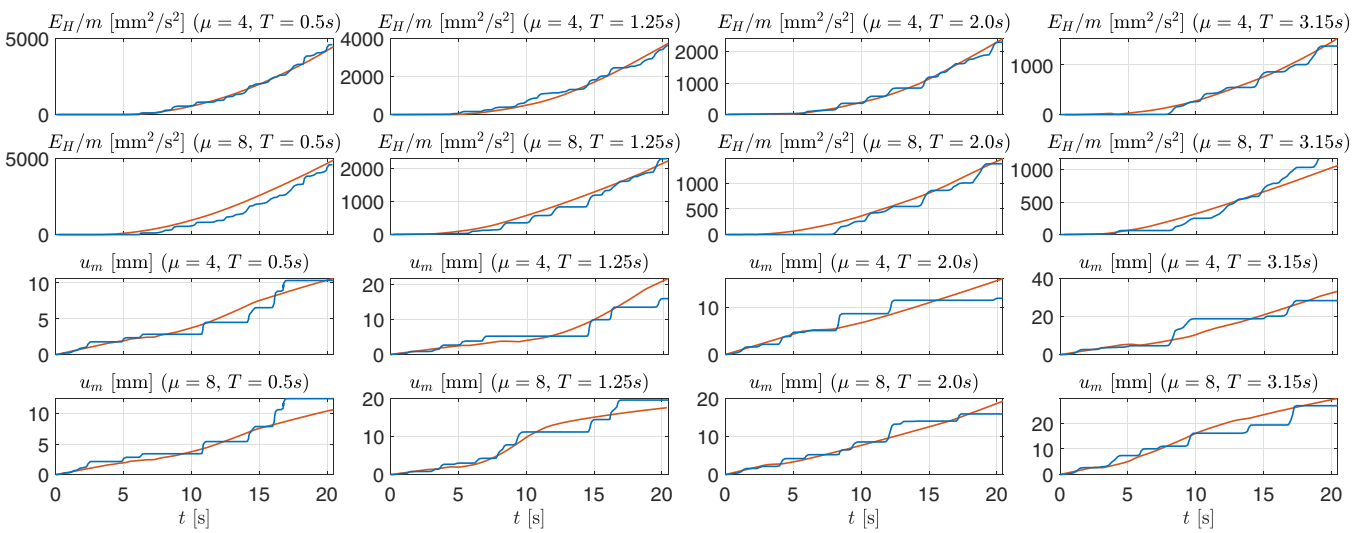
The selected period range reflects the intended scope of the generated IAA, which is ground-motion-dependent rather than structure-dependent. Accordingly, the range of 0.02–5.00 s is not restricted to the fundamental-period range of the dam considered herein; the dam serves as a complex validation case



10969845, 0, Downloaded from https://onlinelibrary.wiley.com/doi/10.1002/eqe.70292 by National Institute Of Stds and Technology, Wiley Online Library on [02/11/2026]. See the Terms and Conditions (https://onlinelibrary.wiley.com/terms-and-conditions) on Wiley Online Library for rules of use; OA articles are governed by the applicable Creative Commons License




(a) Frequency-dependent comparison




(b) Time-dependent comparison

**FIGURE 3** | Comparison of elastic acceleration, elastic / inelastic displacement spectra, nonlinear displacement, and hysteretic energy from target ground motion and the optimized IAA for the horizontal component.

rather than the sole intended application. When such a broad interval is considered, sufficient discretization density is important for maintaining spectral accuracy. The 120 logarithmically spaced period points used herein provide adequate resolution across the selected interval and allow the IAA to reproduce the target ground-motion response spectrum with satisfactory fidelity, as shown in Figure 3. This structure-independent formulation also facilitates the future development of reusable libraries of record-specific IAAs for application to structural systems with different dynamic characteristics.

In addressing the structural ductility aspects relevant to seismic analysis, particularly for concrete dams, this study emphasizes the application of IAAs across a variety of structural forms. Recognizing the inherent differences in ductility demands between building, bridges, and gravity dams, our investigation delineates a clear distinction in their respective ductility characteristics. Unlike framed structures, which are designed for higher ductility to absorb and dissipate seismic energy, (mass) concrete dams, owing to their mass and design criteria, exhibit inherently lower ductility ratios. To ensure the broad applicability and relevance of the IAAs developed herein, we optimized these accelerations for ductility levels of 2, 4, and 8, catering to a wide spectrum of structural requirements.

A comprehensive review of existing literature and detailed analyses of capacity curves for both gravity and arch dams have informed our approach. Figure 4 summarizes representative



10969845, 0, Downloaded from https://onlinelibrary.wiley.com/doi/10.1002/eqe.70292 by National Institute Of Stds and Technology, Wiley Online Library on [02/11/2026]. See the Terms and Conditions (https://onlinelibrary.wiley.com/terms-and-conditions) on Wiley Online Library for rules of use; OA articles are governed by the applicable Creative Commons License

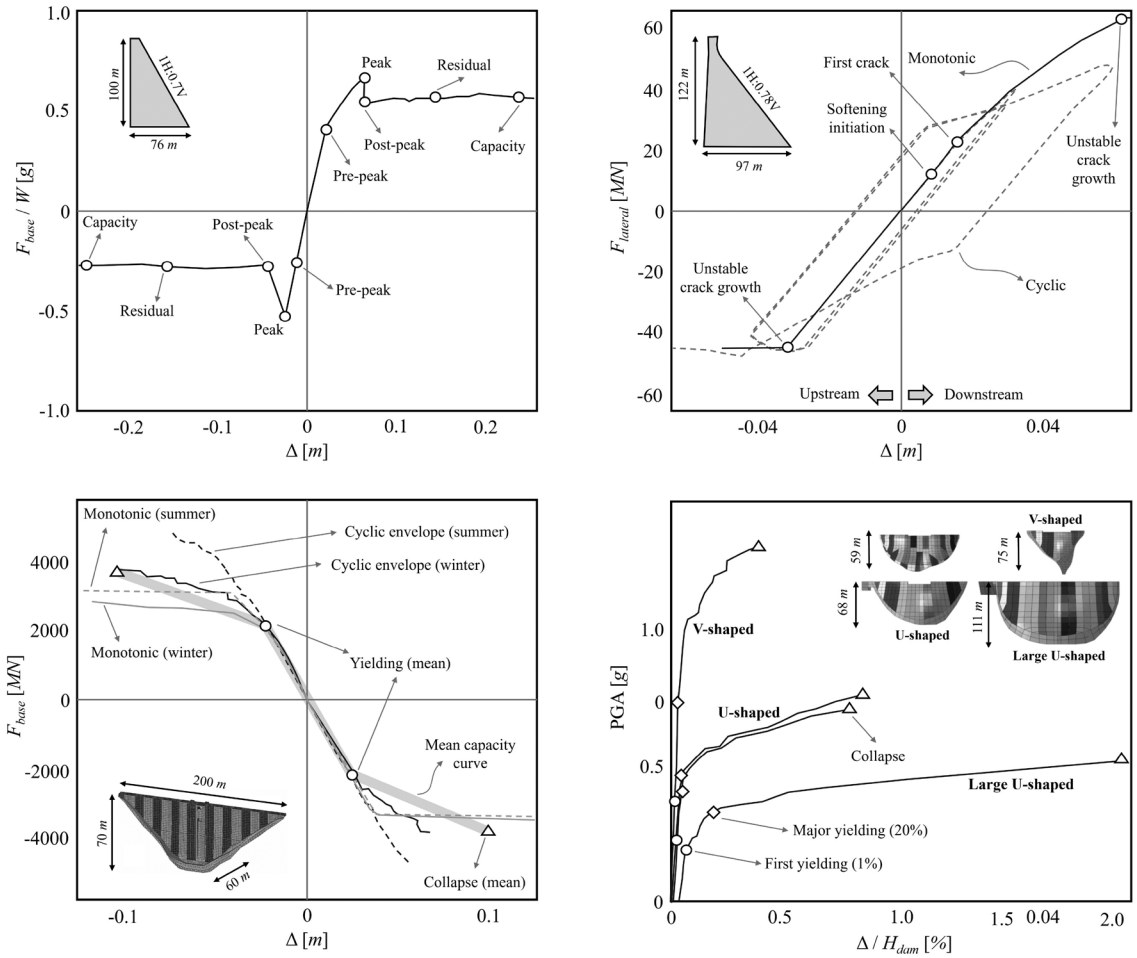



**FIGURE 4** | Capacity curves for concrete dams using monotonic or cyclic pushover methods, or dynamic analysis including the limit state points. The curves are adopted and changed from [13, 14, 63, 64].

capacity curves reported in previous studies to illustrate how ductility-type concepts can be interpreted for concrete dams. These examples include three gravity dams analyzed using two- and three-dimensional finite element models and four arch dams with different geometrical configurations. The capacity curves were obtained under different loading protocols, including monotonic loading, cyclic loading, and dynamic excitation, and draw upon the work of [14], who studied an idealized two-dimensional gravity dam section; [13], who investigated the two-dimensional Pine Flat gravity dam section; [63], who performed a three-dimensional gravity dam analysis; and [64], who examined concrete arch dams with different shapes and sizes.

The four subfigures highlight different but complementary interpretations of dam capacity. Figure 4a shows an idealized gravity dam response in terms of normalized base force versus displacement. The curve identifies representative points such as pre-peak response, peak resistance, post-peak degradation, residual resistance, and final capacity. Figure 4b shows the Pine Flat gravity dam response, where first cracking, softening initiation, and unstable crack growth can be related to changes in the force–displacement curve under monotonic and cyclic loading. Figure 4c presents a three-dimensional gravity dam capacity curve, where temperature-dependent monotonic and cyclic envelopes are combined to define mean yielding and collapse-capacity points. Finally, Figure 4d shows intensity–drift capacity curves for several arch dam geometries, where the response is expressed in terms of PGA and normalized crest displacement; first yielding, major yielding, and collapse are identified as characteristic limit points.

Despite the differences, all four curves share a common interpretation in terms of initial response, nonlinear transition, peak or yielding point, post-peak degradation, residual capacity, and collapse. The derived ductility ratios range from 2 to 4 for gravity dams and potentially higher for arch dams due to their distinct failure modes. These findings substantiate the chosen optimization criteria for the IAAs, ensuring their compatibility with the ductility profiles characteristic of concrete dam structures. By aligning the IAAs with these empirically derived ductility values, we bolster the confidence in their application.

## 2.3 | Connection to PBEE

The proposed record-specific IAA procedure can be integrated into the performance-based earthquake engineering (PBEE) framework as a computationally efficient substitute for single-record IDA. In the conventional PBEE formulation, seismic risk is evaluated by combining seismic hazard, structural response,



10969845, 0, Downloaded from https://onlinelibrary.wiley.com/doi/10.1002/eqe.70292 by National Institute Of Stds and Technology, Wiley Online Library on [02/11/2026]. See the Terms and Conditions (https://onlinelibrary.wiley.com/terms-and-conditions) on Wiley Online Library for rules of use; OA articles are governed by the applicable Creative Commons License

damage, and loss models [65]. In its general form, the mean annual frequency of exceeding a decision variable $DV$ can be expressed using the PEER integral as

$$\lambda(DV) = \iiint G(DV \mid DM)\,|dG(DM \mid EDP)||dG(EDP \mid IM)| \times |d\lambda(IM)|, \tag{17}$$

where $IM$ is the intensity measure obtained from probabilistic seismic hazard analysis (PSHA), $EDP$ is the engineering demand parameter, $DM$ is the damage measure, $DV$ is the decision variable, $G(\cdot)$ denotes a complementary cumulative distribution function, and $\lambda(IM)$ is the seismic hazard curve. When the objective is limited to estimating the annual mean rate of exceeding a structural limit state $LS$, the formulation can be written as

$$\lambda_{LS} = \int_0^\infty \mathbb{P}(LS \mid IM = im)|d\lambda_{IM}(im)|. \tag{18}$$

For a scalar IM with a differentiable hazard curve, Equation (18) can also be expressed as $\lambda_{LS} = \int_0^\infty \mathbb{P}(LS \mid IM = im)\left|\frac{d\lambda_{IM}(im)}{d\,im}\right| d\,im$. Therefore, once the structural fragility function $\mathbb{P}(LS \mid IM = im)$ is available, it can be convolved with the hazard curve from PSHA to estimate the annual mean rate or mean return period of exceeding the selected limit state.

In conventional IDA, the fragility term $\mathbb{P}(LS \mid IM = im)$ is estimated by analyzing a suite of ground motion records scaled to multiple intensity levels. For each record $j$, IDA generates an intensity–demand curve,

$$\mathrm{EDP}_j^{\mathrm{IDA}}(im), \qquad im = IM, \tag{19}$$

from which the exceedance of a limit state threshold $edp_{LS}$ can be evaluated as

$$\mathbb{P}(LS \mid IM = im) = \mathbb{P}(\mathrm{EDP} \geq \mathrm{edp}_{LS} \mid IM = im). \tag{20}$$

The proposed IAA approach preserves this logic, but replaces the repeated scaled analyses of each record with a single analysis using a record-specific IAA. After PSHA is completed, the analyst selects a suite of ground motion records using standard procedures, such as hazard-consistent record selection, conditional spectrum selection, or other site-specific approaches. For each selected record, a corresponding record-specific IAA is generated. The IAA is then analyzed once, and the response is mapped from IAA time to the corresponding ground motion scale factor through

$$SF = \frac{t_{\mathrm{sf}}}{t_{\mathrm{trg}}}, \tag{21}$$

where $t_{\mathrm{trg}}$ is the target time used in IAA generation and $t_{\mathrm{sf}}$ is the IAA mapping time. The corresponding IM value is obtained as

$$IM_j(t_{\mathrm{sf}}) = SF(t_{\mathrm{sf}})\,IM_j(SF = 1). \tag{22}$$

Thus, the IAA analysis provides an approximate intensity–demand curve,

$$EDP_j^{IAA}\big(IM_j(t_{\mathrm{sf}})\big), \tag{23}$$

analogous to the single-record IDA curve but obtained from one intensifying analysis rather than multiple scaled dynamic analyses.

For a suite of $N$ selected ground motion records, the corresponding $N$ record-specific IAAs can be used to estimate the conditional probability of exceeding a limit state as

$$\widehat{\mathbb{P}}(LS \mid IM = im) = \frac{1}{N}\sum_{j=1}^{N} \mathbb{I}\Big[\mathrm{EDP}_j^{\mathrm{IAA}}(im) \geq \mathrm{edp}_{LS}\Big], \tag{24}$$

where $\mathbb{I}[\cdot]$ is the indicator function. Alternatively, the resulting limit-state data can be fitted using a parametric fragility model, such as a lognormal fragility function [66],

$$\mathbb{P}(LS \mid IM = im) = \Phi\left(\frac{\ln im - \ln \theta_{LS}}{\beta_{LS}}\right), \tag{25}$$

where $\theta_{LS}$ is the median capacity, $\beta_{LS}$ is the logarithmic dispersion, and $\Phi(\cdot)$ is the standard normal cumulative distribution function. This fragility function can then be combined with the PSHA hazard curve using Equation (18) to compute the mean annual frequency of exceeding the limit state.

For vector-valued IMs, such as those involving horizontal and vertical components, the same concept applies but the scalar hazard curve is replaced by a vector-valued hazard representation. In that case, $\lambda_{LS} = \int_{\mathbf{IM}} \mathbb{P}(LS \mid \mathbf{IM} = \mathbf{im})\,|d\lambda_{\mathbf{IM}}(\mathbf{im})|$, where $\mathbf{IM}$ may include multiple horizontal and vertical intensity measures. The proposed multi-component IAA framework is compatible with this formulation because each record-specific IAA can be generated for the corresponding horizontal and vertical components of the selected ground motion record.

It is important to emphasize that the proposed IAA procedure does not replace PSHA, hazard characterization, or ground motion selection. Rather, it enters the PBEE workflow after the hazard analysis and record selection steps have been completed. In this setting, the role of IAA is to provide a computationally efficient approximation of the single-record IDA curves needed to construct multi-record fragility functions.

The computational efficiency of IAA is accompanied by an upfront generation cost. A record-specific IAA requires approximately 3–10 h to generate, depending on the ground-motion characteristics and duration, optimization settings, and computing resources. However, this is a one-time, record-dependent cost: once generated, the IAA can be reused for different structural systems. Publicly available IAA libraries, analogous to existing ground-motion databases, could further eliminate this cost for individual users.

## 3 | Case Study Problem

The selected case study for this paper is the Pine Flat concrete gravity dam. This dam holds significant prominence as a benchmark within dam engineering. Notably, it has undergone analysis by the United States Society of Dams (USSD) [67] and the International Committee on Large Dams (ICOLD) [61, 68] in workshops conducted in 2018 and 2019, respectively. In addition to the papers



10969845, 0, Downloaded from https://onlinelibrary.wiley.com/doi/10.1002/eqe.70292 by National Institute Of Stds and Technology, Wiley Online Library on [02/11/2026]. See the Terms and Conditions (https://onlinelibrary.wiley.com/terms-and-conditions) on Wiley Online Library for rules of use; OA articles are governed by the applicable Creative Commons License

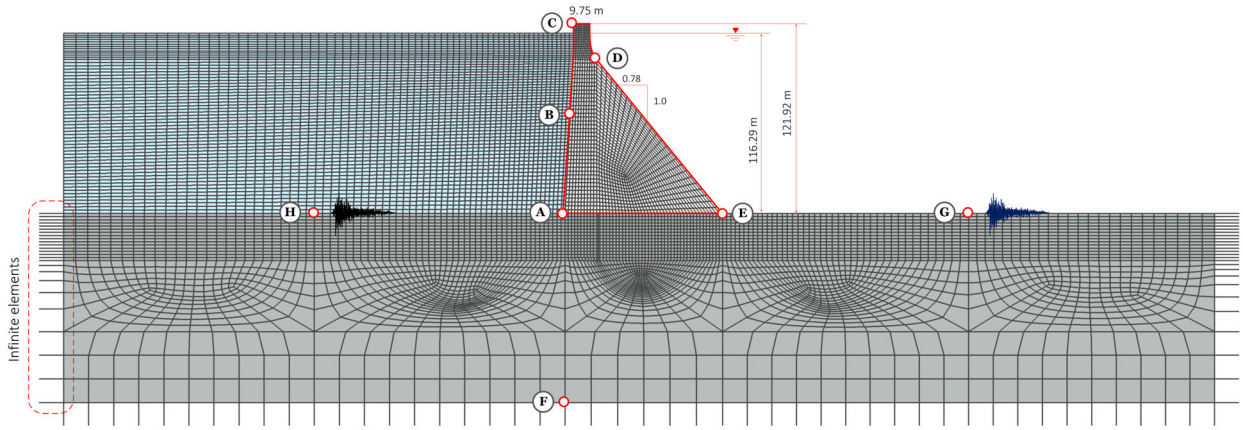



**FIGURE 5** | Finite element model of dam-reservoir-foundation system, including dimensions, foundation boundary conditions, and the location of index points.

discussed in the Introduction Section concerning the application of IAA in dam engineering, the ICOLD proceedings have featured more than ten papers on this subject [69]. Furthermore, the Pine Flat dam has been the subject of extensive study during the 1970s and 1980s at the University of California at Berkeley [70–73].

### 3.1 | FE Model From ICOLD Benchmark

A two-dimensional finite element model representing the central non-overflow section of the Pine Flat dam is constructed in ABAQUS 6.14 [74]. This finite element model encompasses a dam with a height of 121.9 m and a foundation block measuring 700 m in length and 122 m in depth, along with a reservoir segment spanning 310 m in length and 116 m in depth. The foundation is simulated as a linear elastic domain, comprising 4520 four-node plane-stress elements, while the dam body consists of 1391 four-node plane-stress elements. The plane-stress formulation is adopted for the entire coupled dam–foundation system to maintain a consistent two-dimensional element idealization, following similar Abaqus-based dam–foundation modeling studies [75]. Although plane-strain can also be appropriate for the foundation rock because of its out-of-plane continuity, the present study focuses on the responses in the dam body, and no foundation stress distribution is interpreted.

Additionally, the reservoir is depicted using 4012 four-node bilinear acoustic elements to account for compressible media. The pressure within the acoustic elements exclusively represents hydrodynamic effects, necessitating the direct application of an equivalent hydrostatic pressure at the interfaces between acoustic and solid domains, that is, dam or foundation. At the upper surface of the acoustic domain, a zero-pressure condition is enforced. At the truncated far-end boundary of the reservoir, low-reflecting boundary conditions [76] are applied using the acoustic surface-impedance/nonreflecting boundary option in ABAQUS to represent the reservoir's unbounded nature. Figure 5 illustrates the finite element model including the key nodes from which results will be extracted and subsequently discussed.

The implicit time integration method is utilized to calculate the transient response of the dam-foundation-reservoir system. Given the structural problem's nature, involving substantial energy dissipation (such as through plasticity) and the dynamic input's sudden variations in intensity and direction, an automatic time step incrementation scheme is adopted. This scheme employs half-step residual control to ensure the accuracy of the dynamic solution. The half-step residual, representing the equilibrium residual error (or out-of-balance forces) at the midpoint of a time increment, serves as the foundation for this adaptive time incrementation scheme. A small half-step residual indicates high solution accuracy, allowing for a safe increase in the time step. Conversely, a large half-step residual necessitates a reduction in the time step to maintain solution integrity. The analysis parameters, including the chosen time steps and tolerance levels for the balance equations and nodal variable corrections, are summarized in Table 1. This table outlines the initial suggested time step, minimum and maximum time step values, and the criteria for error tolerance, aligning the time step settings with the characteristics of the ground motion record to ensure fidelity in seismic input representation.

**TABLE 1** | Specifications for numerical simulation.

| Parameter | Value |
|---|---|
| Suggested time step | 0.01 [s] |
| Minimum time step | 1e-7 [s] |
| Maximum time step | 0.01 [s] |
| Error on residuals in balance equations for displacement field ≤ | 5e-3 |
| Largest correction to nodal variables by each Newton iteration ≤ | 1e-2 times the largest change in nodal variable in the increment |

### 3.2 | SSI and Deconvolution

Two distinct approaches are employed for modeling the foundation: the massless model and the massed model. While the former is commonly used by practitioners, the latter is widely regarded as more accurate within the scientific community [76, 77]. SSI comprises two main contributions: kinematic interaction and



10969845, 0, Downloaded from https://onlinelibrary.wiley.com/doi/10.1002/eqe.70292 by National Institute Of Sids and Technology, Wiley Online Library on [02/11/2026]. See the Terms and Conditions (https://onlinelibrary.wiley.com/terms-and-conditions) on Wiley Online Library for rules of use; OA articles are governed by the applicable Creative Commons License

inertial interaction [78]. The former is determined by soil/rock flexibility, while the latter arises from elastic waves generated under dynamic loads, fostering energy transmission across the soil/rock volume. This phenomenon, which carries energy away from the structure, is often termed "radiation damping".

In seismic analysis with a massless model, inertial interaction is entirely neglected. The wave velocity within the foundation becomes infinite, and the seismic input applied at the domain's boundaries instantaneously reaches the structure's base, absorbing all kinetic energy [79]. These two distinct modeling strategies profoundly impact the dynamic analysis results [76]. It is crucial to choose appropriate boundary conditions and pre-process the seismic input to ensure comparability between these two assumptions.

For this study, the ABAQUS built-in infinite elements are utilized to simulate the soil/rock domain's unbounded nature. The dynamic implementation of these infinite elements (following [80]) shares a similar formulation with traditional finite elements, except for the infinite extent of the element region and shape function in one direction. Further details can be found in [81]. In addition to addressing the unboundedness of the soil/rock domain, the massed model requires additional consideration of the seismic input. The inertial component of SSI results in higher damping, reducing the seismic input. A massed soil/rock acts as a filter for this input, implying that when both the massless and massed foundation models experience identical dynamic excitation at the foundation domain's bottom (point F in Figure 5), the recorded acceleration at the free surface (point G) varies between them. Consequently, the seismic input of the massed foundation model has then to be deconvolved to achieve acceleration at point G similar to that of the massless model. A comprehensive deconvolution process is explained in [82]. The Rayleigh damping formulation with 2% of critical damping values is employed. Only the stiffness proportional part is considered, utilizing a proportionality factor of $\beta_K$ equal to 0.0022 and 0.0044 for concrete and rock, respectively. Accordingly, the effective modal damping ratio is frequency-dependent, that is, $\xi_i = \beta_K \omega_i / 2$ for each mode $i$, and therefore varies across the lower modes of the dam–reservoir–foundation system rather than remaining exactly constant at 2%.

**TABLE 2** | Elastic and damage plasticity properties of concrete and rock foundation. Adapted from [61, 68, 84]

| Material and/or model properties | Symbol | Quantity |
|---|---|---|
| Concrete unit weight | $\rho_c$ | 2,483 kg/m$^3$ |
| Concrete elastic moduli | $E_c$ | 22,410 MPa |
| Concrete Poisson's ratio | $\upsilon_c$ | 0.2 |
| Dilation angle | $\Psi$ | 36.31° |
| Eccentricity to define the rate at which the flow potential approaches the asymptote | $\varepsilon$ | 0.1 |
| Ratio of initial equi-biaxial compressive to initial uniaxial compressive yield stress | $\frac{\sigma_{b0}}{\sigma_{c0}}$ | 1.16 |
| Ratio of the second stress invariant on the tensile meridian to that on the compressive meridian | $\Lambda$ | 0.66 |
| Concrete tensile strength | $f_t$ | 2 MPa |
| Concrete compressive strength | $f_c$ | 20 MPa |
| Fracture energy (tensile) | $G_f$ | 250 N/m |
| Rock unit weight | $\rho_r$ | 2,483 kg/m$^3$ |
| Rock elastic moduli | $E_r$ | 22,410 MPa |
| Rock Poisson's ratio | $\upsilon_r$ | 0.2 |
| Water unit weight | $\rho_w$ | 1,000 kg/m$^3$ |
| Compression wave velocity | $c_p$ | 1,439 m/s |

### 3.3 | Material Properties and Concrete Damage

Depending on the analysis type, either a linear elastic or a nonlinear damage model is applied to the dam body. The elastic properties of concrete and the rock foundation are summarized in Table 2. The nonlinear behavior of the dam is simulated using the concrete damage plasticity constitutive model [83]. This model has been widely adopted in structural and dam engineering [17] due to its capability to accurately represent the response of non-reinforced concrete under cyclic loading. The concrete damage plasticity model necessitates defining the concrete's post-elastic behavior, both in compression and tension, along with plastic flow parameters. Specifically, the tensile post-elastic behavior is characterized by a descending exponential function, while the compressive post-elastic behavior can be described by both a hardening and a softening segment [3]. The development of micro-cracks, leading to concrete damage, is simulated by reducing the elastic modulus through the scalar value $d_t$, which is a function of plastic deformation. In the present model, the dam–foundation interface is assumed to be perfectly bonded, and no explicit nonlinear interface joint is introduced. This modeling choice was made to focus on one dominant nonlinear mechanism, namely continuum damage in the dam body, and to keep the comparison between IDA and IAA responses transparent.

## 4 | Results: IAA versus Single-Record IDA

Upon completion of the finite element model setup, initial simulations were conducted to validate the model's results against the ICOLD benchmark problem [61, 68]. The first three natural frequencies of the model were determined to be 2.05 Hz, 3.11 Hz, and 3.42 Hz, respectively. These frequencies align closely with the ICOLD benchmark averages and their associated standard deviations: 2.15±0.34 Hz, 3.28±0.63 Hz, and 3.91±0.79 Hz. Such comparisons validate the accuracy of the model's first three modes against the established benchmark. Further validation was performed by comparing dynamic analysis outcomes, using the normal water level and the unscaled Taft ground motion record, against the benchmark's mean response. The results, specifically in terms of peak horizontal acceleration and crest displacement, exhibit close agreement with the mean responses from the benchmark and fall within the range of mean ±



10969845, 0, Downloaded from https://onlinelibrary.wiley.com/doi/10.1002/eqe.70292 by National Institute Of Stds and Technology, Wiley Online Library on [02/11/2026]. See the Terms and Conditions (https://onlinelibrary.wiley.com/terms-and-conditions) on Wiley Online Library for rules of use; OA articles are governed by the applicable Creative Commons License

one standard deviation. Given the favorable consistency of the results, the adopted finite element model in this study is deemed sufficiently reliable.

### 4.1 | Comparison of IAA and IDA Capacity Curves

A series of transient simulations are conducted using both the real ground motions at various scale factors and the generated IAAs (as shown in Figure 2b). As discussed previously, the primary aim of this study is to validate the IAA method against the corresponding single-record IDA. To ensure the generalizability of results across different structural systems and foundation types (i.e., wave propagation models), four distinct scenarios are considered in this paper: (1) linear elastic system with a massless foundation (no wave propagation, no deconvolution), (2) linear elastic system with a massed foundation (includes wave propagation, requires deconvolution), (3) non-linear damage model with a massless foundation, and (4) non-linear damage model with a massed foundation.

The IDA method was initially developed to explore the non-linear behavior of structures [85] under seismic excitation by incrementing a scale factor applied to the reference ground motion until the structure approaches theoretical failure. Although the scale factor can be increased using constant increments (a simpler approach), alternatives like the hunt&fill method [85], which optimizes the process, are available. In this paper, the hunt&fill method is employed for conducting IDA analyses, requiring ten transient simulations for each IDA curve. For nonlinear massless (and massed) foundation models, the following scale factors were determined by the algorithm: 1.00 (1.00), 1.57 (1.99), 0.50 (1.49), 1.28 (0.50), 0.25 (1.74), 0.75 (1.24), 1.42 (0.25), 1.14 (0.75), 0.87 (0.37), 0.37 (0.38). However, linear elastic models lack a theoretical failure point. In aligning our analysis approach with that used for nonlinear models, we conducted a series of ten simulations for the linear models, employing varying scale factors for the ground motion. It is critical to acknowledge that, in theory, a purely linear elastic system necessitates only two simulations to define the capacity curve, as any subsequent simulations would inherently align with this established linear trajectory. However, the significance of pre-dynamic structural responses in the comparative analysis of IAA and IDA cannot be overstated. Initial pre-seismic loadings, such as substantial thermal stresses or strains induced by alkali-silica reaction, could significantly alter the system's behavior. Specifically, if such loading nudges the system toward nonlinear behavior or approaches its yield threshold, the analysis context shifts. Despite these complexities, the expectation remains that IAA should align with the IDA during the dynamic phase of analysis.

In each of the four scenarios discussed in this paper, 11 analyses are performed (10 simulations for IDA using 10 scaled records and one IAA). The IDA curve is generated by connecting the peak responses from various scaled records and plotting them against the seismic intensity of the scaled record. Various approaches can be used for this purpose, including piecewise linear interpolation, spline interpolation, and the Ramberg-Osgood equation. For this paper, the linear interpolation approach is utilized. The resulting IDA curve, representing the relationship between EDP and IM, is typically referred to as a capacity function.

Generating the capacity function using the IAA involves a distinct procedure. The response time history, such as the displacement, EDP($t$), is recorded. It's important to acknowledge that in nonlinear systems, certain analyses may fail at specific time points, $t_{\text{fail}}$, either due to numerical non-convergence or physical failure (e.g., exceeding a displacement threshold). The maximum absolute EDP value is then calculated at any time $\tau$ using the following operator:

$$\Omega(t) = \max_{\tau \in [0,t]} |EDP(\tau)|. \tag{26}$$

This results in a step-wise increasing function in the time-EDP coordinate system. To enable a comparison of the results with those from IDA, both should share the same coordinate system. Hence, the "time" parameter in IAA must be converted into a suitable IM parameter. This is achieved by utilizing the truncated acceleration within the time interval $[0, \tau]$ to compute the IM parameter corresponding to time $\tau$. The outcome is a step-wise capacity function within the IM-EDP coordinate system, facilitating a direct comparison with the IDA results.

To facilitate a meaningful comparison between capacity functions obtained through IAA and IDA, two sets of quantitative metrics are chosen: similarity measures and distance metrics [86]. Let's consider two time series, denoted as vectors $A$ and $B$, each of length $n$. The $i$-th values of $A$ and $B$ are represented as $a_i$ and $b_i$, respectively. Additionally, let's define the similarity between two scalars $a$ and $b$ as $sim(a,b) = 1 - \frac{|a-b|}{|a|+|b|}$. Subsequently, various distance metrics, $d(A,B)$, and the similarity between two time-series $A$ and $B$ can be computed as follows:

$$\begin{cases}
d_{\text{euc}} = \sqrt{\sum_{i=1}^{n} (a_i - b_i)^2}, & \text{Euclidean Distance} \\
d_{\text{mah}} = \sum_{i=1}^{n} |a_i - b_i|, & \text{Manhattan Distance} \\
d_{\text{max}} = \max_{0<i\le n} |a_i - b_i|, & \text{Maximum Distance} \\
d_{\text{mnk}} = \left( \sum_{i=1}^{n} |a_i - b_i|^p \right)^{1/p}, & \text{Minkowski Distance} \\
t_{\text{sim}} = \frac{1}{n} \sum_{i=1}^{n} \text{sim}(a_i, b_i), & \text{Mean similarity} \\
rt_{\text{sim}} = \sqrt{\frac{1}{n} \sum_{i=1}^{n} \text{sim}(a_i, b_i)^2}, & \text{RMS similarity} \\
p_{\text{sim}} = \frac{1}{n} \sum_{i=1}^{n} \left( 1 - \frac{|a_i - b_i|}{2 \max(|a_i|, |b_i|)} \right), & \text{Peak similarity} \\
\rho_{\text{Pearson}} = \frac{\sum_{i=1}^{n} (a_i - \bar{A})(b_i - \bar{B})}{\sqrt{\sum_{i=1}^{n} (a_i - \bar{A})^2} \sqrt{\sum_{i=1}^{n} (b_i - \bar{B})^2}}, & \text{Pearson's corr.} \\
\rho_{\cos} = \frac{\sum_{i=1}^{n} a_i b_i}{\sqrt{\sum_{i=1}^{n} a_i^2} \sqrt{\sum_{i=1}^{n} b_i^2}}, & \text{Cosine of the angle}
\end{cases} \tag{27}$$

All nine (actually ten as the Minkowski distance is computed using both $p$ equal to 3 and 4) similarity metrics are computed



10969845, 0, Downloaded from https://onlinelibrary.wiley.com/doi/10.1002/eqe.70292 by National Institute Of Stds and Technology, Wiley Online Library on [02/11/2026]. See the Terms and Conditions (https://onlinelibrary.wiley.com/terms-and-conditions) on Wiley Online Library for rules of use; OA articles are governed by the applicable Creative Commons License

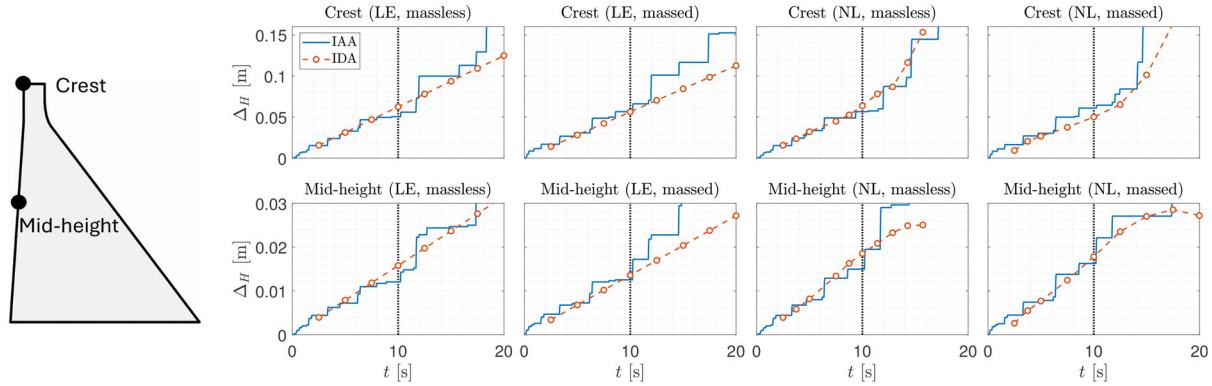



**FIGURE 6** | Comparison of time-dependent peak horizontal displacement from IAA and IDA at two locations and four modeling scenarios.

twice: once for the time (or equivalent intensity) interval $[0, t_f)$, covering the entire duration of the IAA from beginning to the failure time, and once for the interval $[0, t_{trg})$, which focuses only on the time span where the target ground motion may be down-scaled (and not up-scaled). This distinction allows us to assess the influence of non-linearity and damage on the similarity between the IAA and IDA curves.

As both the horizontal and vertical acceleration components are considered in this study, the results are organized into three main categories: (1) vector EDPs in the horizontal direction only (Section "Displacement EDP in Horizontal Direction"), (2) vector EDPs in the vertical direction only (Section "Displacement EDP in Vertical Direction"), and (3) scalar EDPs (covered in Sections "Principal Stresses" and "Damage Index and Crack Profile"). The first and second categories cover the horizontal and vertical displacement responses, respectively, while the third category compares the maximum principal stresses and the damage index.

## 4.2 | Displacement EDP in Horizontal Direction

Figure 6 displays the peak horizontal displacement at two distinct locations: the dam crest (point C) and the mid-height of the upstream face (point B). These results correspond to the four different modeling scenarios. The outcomes for the IAA method are shown in the $t - -\Delta_H$ coordinate system, while the IDA curve is transformed into the "time" domain. For each simulation in IDA, the scale factor is converted into the equivalent time using $t_{SF} = 10 \times SF$ [s] (notably, 10 s corresponds to $t_{trg}$ as discussed in Equation 10). Across both linear and non-linear models, there is a noticeable consistency between the capacity curves derived from IAA and IDA. In nearly all modeling assumptions, there is a precise prediction of the displacement response at the target time, that is, 10 s. Moreover, for non-linear models, both the IDA and IAA-based curves exhibit similar curvatures. Specifically, the capacity curves for crest displacements are concave upward, while for the mid-height location, they are concave downward. This characteristic suggests significant damage to the upper portion of the dam within the time interval $t \in [12, 16]$.

The degree of similarity between the IDA and IAA curves shown in Figure 6 is further quantified through the application of the ten metrics introduced in Equation 27. The comparison between the IDA and IAA curves is conducted in two distinct regions (Figure 7): (1) the down-scaling zone, encompassing $t \in [0, t_{trg})$, where all real ground motions are multiplied by a scale factor less than one, and (2) the full zone, covering $t \in [0, t_f)$, in which real ground motions are both down-scaled and up-scaled until structural failure. This comparison serves to identify whether the similarity is stronger in either zone and to assess whether non-linearity has a detrimental impact on the similarity between IDA and IAA.

In terms of the similarity metrics, it becomes apparent that the massless foundation models exhibit higher values of $t_{\text{sim}}$, $rt_{\text{sim}}$, and $p_{\text{sim}}$ compared to the massed models, whether they are linear or non-linear. Within the context of the massless foundation models, the nonlinear model showcases superior performance relative to the linear elastic model, particularly in the comparison of the full curves. Conversely, in the massed foundation models, the similarity slightly decreases for the nonlinear model, although there is a modest improvement in similarity for the comparison over the full zone. It is important to note that the "peak similarity" and "maximum distance" metrics may yield slightly different outcomes compared to the mean metrics, and careful interpretation of the results is necessary. Among all four modeling scenarios, it appears that the linear elastic model with a massless foundation demonstrates the highest degree of similarity (and lowest distance), while the nonlinear model with a massed foundation yields less similarity.

Figure 8 illustrates the acceleration time history at two distinct locations: the base of the foundation domain (point F) and the free surface of the foundation adjacent to the structure (point A). These locations are chosen to enable a comprehensive examination of the accuracy of acceleration estimation under various conditions. In general, the consistency between IAA and IDA is deemed satisfactory for all the considered modeling assumptions. Discrepancies noted at higher times ($t > 12$ s), corresponding to higher acceleration levels, arise from significant acceleration spikes in IAA, leading to pronounced steps. Smoothing the IAA curve can mitigate these local discrepancies, enhancing the alignment of IAA with IDA across both the top and bottom foundation index points.

Figures 6 and 8 are time-EDP and time-IM capacity curves. Therefore, the parameter "time" is excluded, and the direct IM-EDP capacity curves are presented in Figure 9. In this case,



10969845, 0, Downloaded from https://onlinelibrary.wiley.com/doi/10.1002/eqe.70292 by National Institute Of Stds and Technology, Wiley Online Library on [02/11/2026]. See the Terms and Conditions (https://onlinelibrary.wiley.com/terms-and-conditions) on Wiley Online Library for rules of use; OA articles are governed by the applicable Creative Commons License

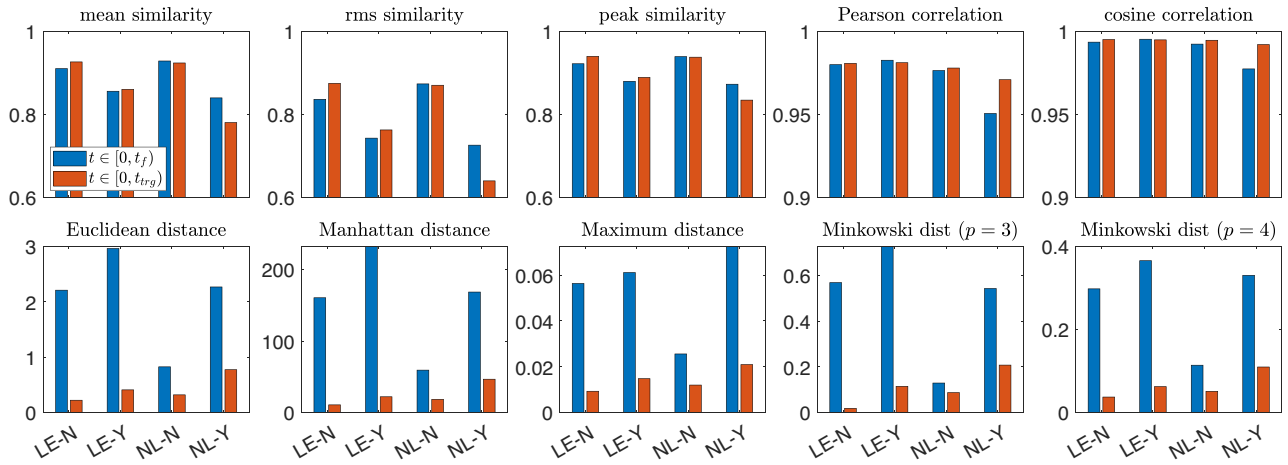



**FIGURE 7** | Quantification of similarity between IAA and IDA curves for crest horizontal displacement, and four modeling scenarios. Metrics are provided in two zones: up to target time, and the entire simulation duration. LE: linear elastic, NL: non-linear, N: massless foundation, Y: massed foundation.

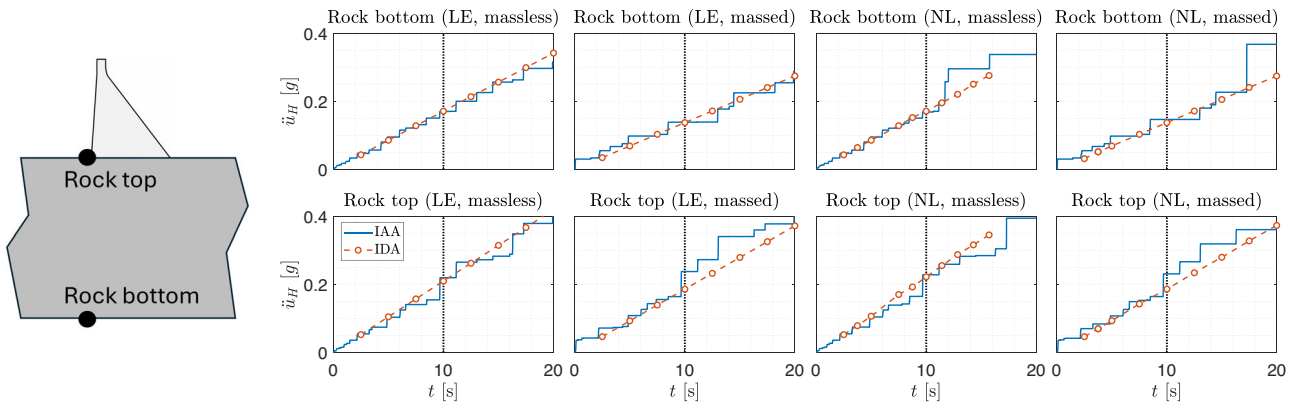



**FIGURE 8** | Comparison of peak recorded (total) accelerations from IAA and IDA at the bottom and top of the foundation for four modeling scenarios.

the EDP is the crest horizontal displacement, $\Delta_H$, while three alternative IMs are examined to find the optimal:

- $\text{ZPA}_H$: zero-period acceleration (equivalent to PGA), typically measures the peak acceleration and ignores the spectral shape.
- $S_{a,H}(T_1)$: first-mode spectral acceleration, which accounts for spectral value in one specific period, and is appropriate for first-mode dominant structures.
- $\bar{S}_{a,H}^{[\alpha,\beta]}(T_1)$: normalized spectral acceleration at the period range of $[\alpha T_1, \beta T_1]$ ($\alpha = 0.2$ and $\beta = 2$). It accounts for spectral shape and is particularly effective for nonlinear systems in which the potential damage shifts the dominant period of the system toward a larger value [87].

The initial IM parameters are all based on the horizontal component of ground motion or IAA. This choice is due to the fact that the EDP is selected as $\Delta_H$. However, in practice, the dam-foundation system experiences both the horizontal and vertical components of shaking, and their combined effect also needs to be investigated as an alternative IM. Therefore, six additional combined IM parameters are defined, as illustrated in Figure A2 in appendix. These additional IMs are constructed by combining the aforementioned three initial IMs using one of the following techniques [88]:

- $\text{IM}_{\text{art}} = \frac{1}{2}(\text{IM}_H + \text{IM}_V)$ arithmetic mean
- $\text{IM}_{\text{geo}} = (\text{IM}_H \times \text{IM}_V)^{1/2}$ geometric mean
- $\text{IM}_{\text{wgeo}} = \left(\text{IM}_H^2 \times \text{IM}_V\right)^{1/3}$ weighted geometric mean
- $\text{IM}_{\text{srss}} = \left(\text{IM}_H^2 + \text{IM}_V^2\right)^{1/2}$ square root of the sum of the squares

For all nine IM parameters (including three single-component and six combined ones), the capacity functions derived from IDA and IAA exhibit strong agreement. The curvature of nonlinear models is accurately captured. When using $S_a(T_1)$-based IMs (both single-component and combined versions), there can be noticeable steps in the IAA capacity function, which causes deviations from the IDA curve within certain intensity ranges.



10969845, 0, Downloaded from https://onlinelibrary.wiley.com/doi/10.1002/eqe.70292 by National Institute Of Stds and Technology, Wiley Online Library on [02/11/2026]. See the Terms and Conditions (https://onlinelibrary.wiley.com/terms-and-conditions) on Wiley Online Library for rules of use; OA articles are governed by the applicable Creative Commons License

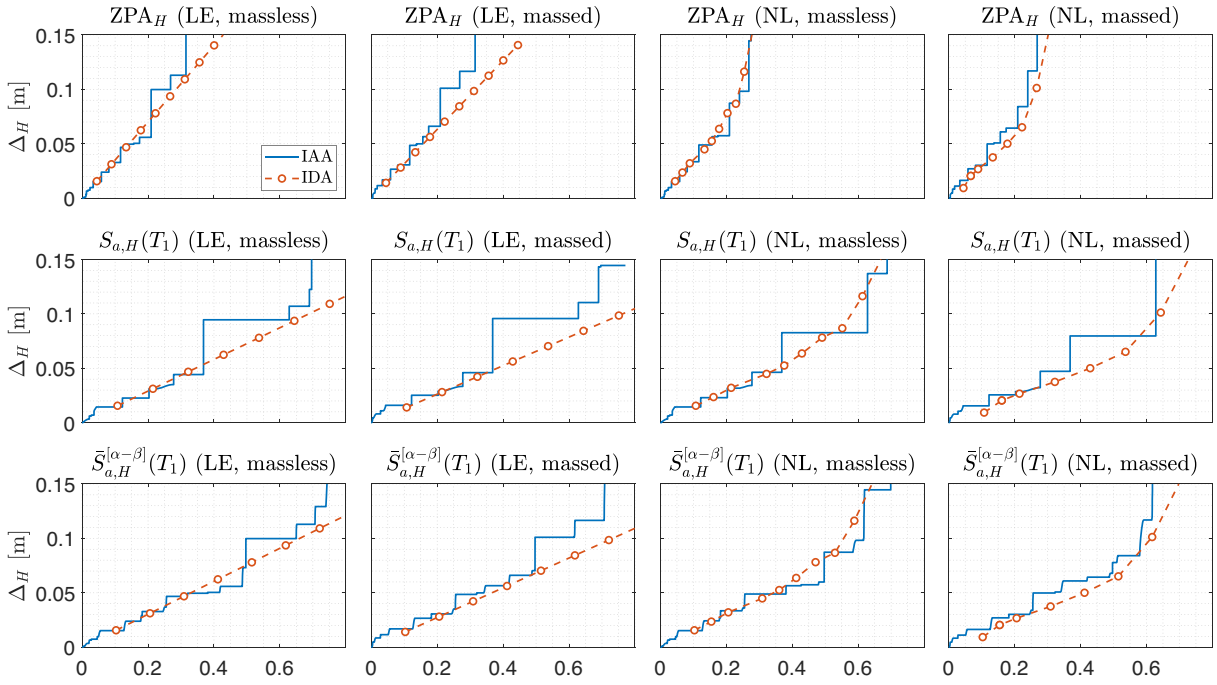
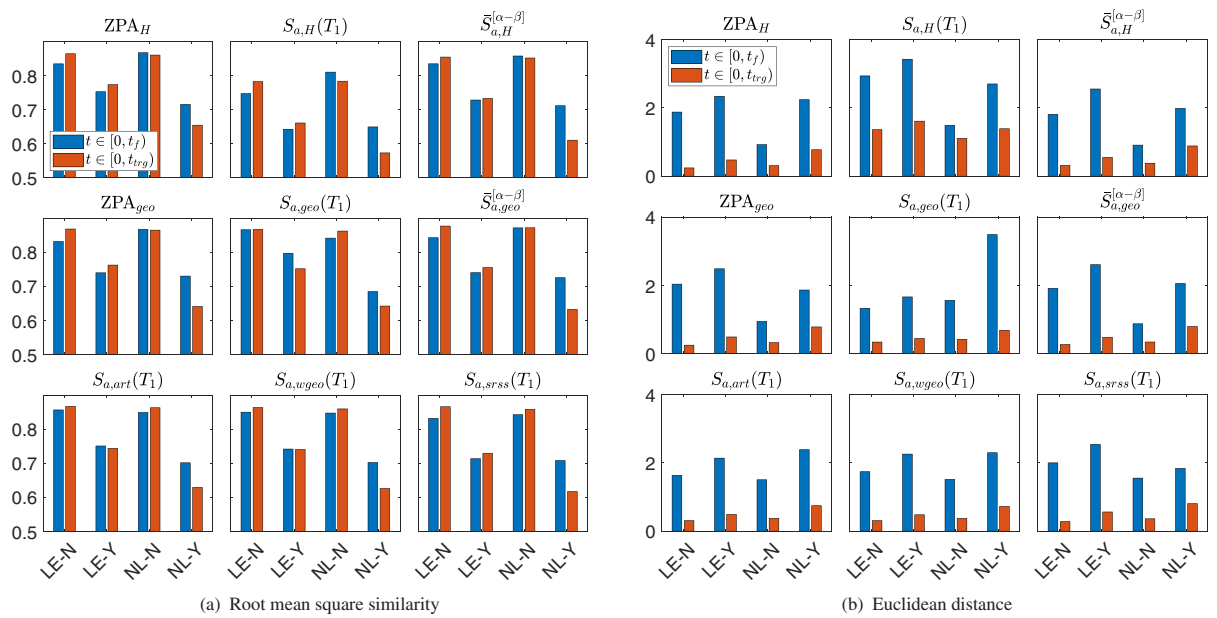



**FIGURE 9** | Direct comparison of IAA and IDA in terms of various horizontal-only IM parameters and a global EDP (i.e., horizontal displacement)




(a) Root mean square similarity

(b) Euclidean distance

**FIGURE 10** | Quantification of similarity between IAA and IDA curves using nine alternative IM parameters. Results are presented for crest displacement, and four modeling scenarios. Metrics are provided for two zones: before target time, and the entire simulation duration.

However, the use of $\bar{S}^{[\alpha,\beta]}_{a}(T_1)$ mitigates this issue, resulting in a smoother capacity function for IAA.

The degree of compatibility between IDA and IAA curves using different IM parameters can be further evaluated through the metrics presented in Equation 27. To simplify the presentation of multiple metrics, only two are considered: the root mean square similarity and the Euclidean distance. Figure 10 quantitatively illustrates the similarity and distance metrics for nine alternative IMs in two specific zones. As the vertical axis in all sub-plots represents $\Delta_H$, a direct comparison across various IMs can be made. Several conclusions can be drawn from the analysis of these results: (1) the choice of any of the nine IMs does not significantly alter the overall trend of the results, (2) among the three horizontal-only IMs, $S_{a,H}(T_1)$ exhibits the least similarity and the largest distance indices. On the other hand, $\bar{S}^{[\alpha,\beta]}_{a,H}(T_1)$ performs better than ZPA$_H$, (3) adopting the geometric mean of the three initial IMs enhances the similarity of $S_{a,\text{geo}}(T_1)$, surpassing the



10969845, 0, Downloaded from https://onlinelibrary.wiley.com/doi/10.1002/eqe.70292 by National Institute Of Stds and Technology, Wiley Online Library on [02/11/2026]. See the Terms and Conditions (https://onlinelibrary.wiley.com/terms-and-conditions) on Wiley Online Library for rules of use; OA articles are governed by the applicable Creative Commons License

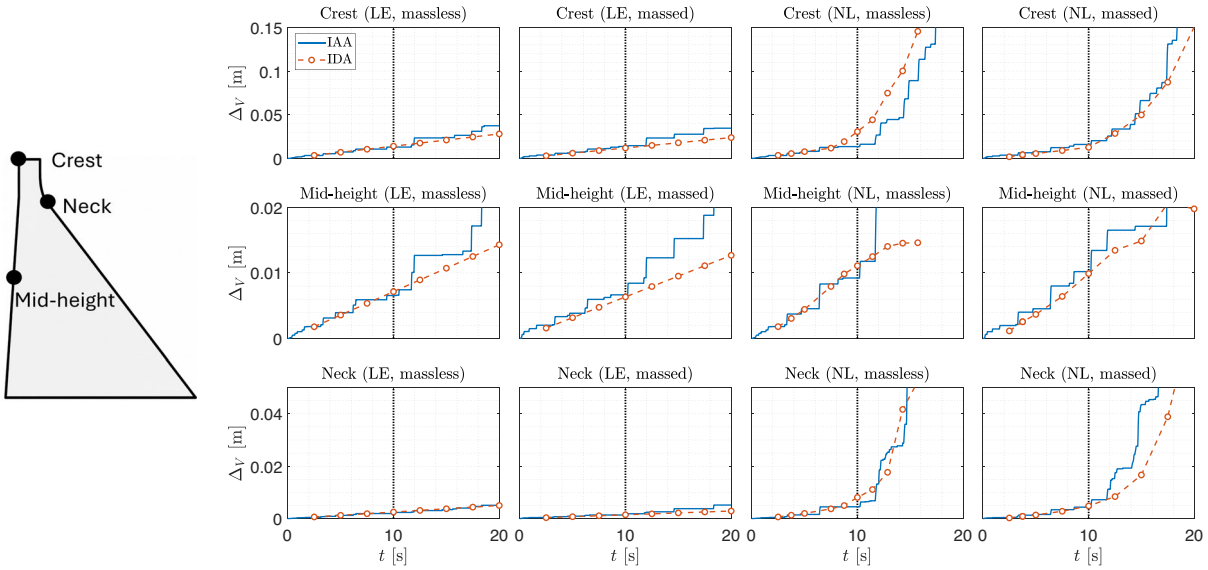



**FIGURE 11** | Comparison of time-dependent peak vertical displacement from IAA and IDA at three locations and four modeling scenarios

performance of the other two IMgeo for linear elastic models. However, for non-linear analyses, $\bar{S}a, \text{geo}^{[\alpha,\beta]}(T_1)$ is the superior choice, (4) the arithmetic, geometric, weighted geometric mean, and SRSS (square-root-of-sum-of-squares) methods provide alternative IM representations under which the measured similarity scores are generally higher and the distance values are generally lower. Among these alternatives, the geometric mean remains the simplest and most effective representation for the cases considered herein, and (5) in most modeling scenarios, except for the nonlinear model with a massed foundation, the similarity of IDA and IAA curves in zone 1 (prior to the target time) is slightly higher than in zone 2, that is, the entire simulation range.

### 4.3 | Displacement EDP in Vertical Direction

The discussion presented in Section "Displacement EDP in Horizontal Direction" primarily focused on horizontal displacements. However, it is equally important to investigate the accuracy of estimated results in the vertical direction for vectorial EDPs like displacement. Figure 11 provides an overview of the peak vertical displacement at three distinct locations: the dam crest (point C), the mid-height of the upstream face (point B), and the downstream neck (point D), across four different modeling scenarios. The results for both IAA and IDA are displayed within the time-$\Delta_V$ coordinate system. Similar to the analysis in Figure 6 that involved horizontal displacement ($\Delta_H$), this figure also demonstrates a consistent alignment between the capacity curves derived from IAA and IDA for both linear and nonlinear models. Notably, when compared to the findings in Figure 6, where $\Delta_H$ was presented, the vertical displacement for the crest and neck locations within non-linear models is substantially larger. This distinction can be attributed to the occurrence of cracking in the neck area, enabling greater movement in the upper sections of the structure.

Figure 12 shows the similarity between the IDA and IAA curves in terms of vertical displacement. The pattern of similarity indices observed in this figure follows the same trend as those identified in the context of horizontal displacement. Notably, the linear massless foundation model showcases higher values for the similarity metrics $t_{\text{sim}}$, $rt_{\text{sim}}$, and $p_{\text{sim}}$ in comparison to the other models. In contrast to the horizontal displacement ($\Delta_H$) analysis, the non-linear model with a massless foundation displays the largest Euclidean distance among the four modeling scenarios. This result indicates that, for the vertical displacement at the crest in this specific modeling case, the IAA-predicted response is generally lower than the corresponding IDA response over part of the non-linear response range.

### 4.4 | Principal Stresses

In the preceding sections, the focus was on investigating vectorial EDPs, separately analyzing the horizontal and vertical directions. Similar discussions and analyses can be extended to other quantities such as velocity, stress, and strain. When it comes to stress response, particularly in linear elastic systems, one of the most significant quantities is the first principal stress, denoted as $\sigma_{p1}$. This parameter is important as it serves as a simple metric for assessing potential damage extent, particularly in relation to crack initiation [89].

For the purpose of stress evolution analysis, the finite element located at point A (refer to Figure 5) is chosen. The time history of $\sigma_{p1}$ for the four integration points associated with this element are compared between IDA and IAA analyses. Figure 13 depicts the outcomes of this stress comparison for two linear elastic systems. It's important to note that integration points in non-linear models are automatically considered as cracked when stress exceeds the failure surface. As a result, this specific comparison is limited to linear analyses only, excluding nonlinear models.

In the plotted figure, the horizontal line corresponds to the concrete tensile strength, designated as $f_t'$. This value serves as a threshold between linear and nonlinear behavior, assuming that triaxial stress effects are not considered. It's noteworthy that $\sigma_{p1}$ represents the magnitude of a tensor quantity without referencing



10969845, 0, Downloaded from https://onlinelibrary.wiley.com/doi/10.1002/eqe.70292 by National Institute Of Stds and Technology, Wiley Online Library on [02/11/2026]. See the Terms and Conditions (https://onlinelibrary.wiley.com/terms-and-conditions) on Wiley Online Library for rules of use; OA articles are governed by the applicable Creative Commons License

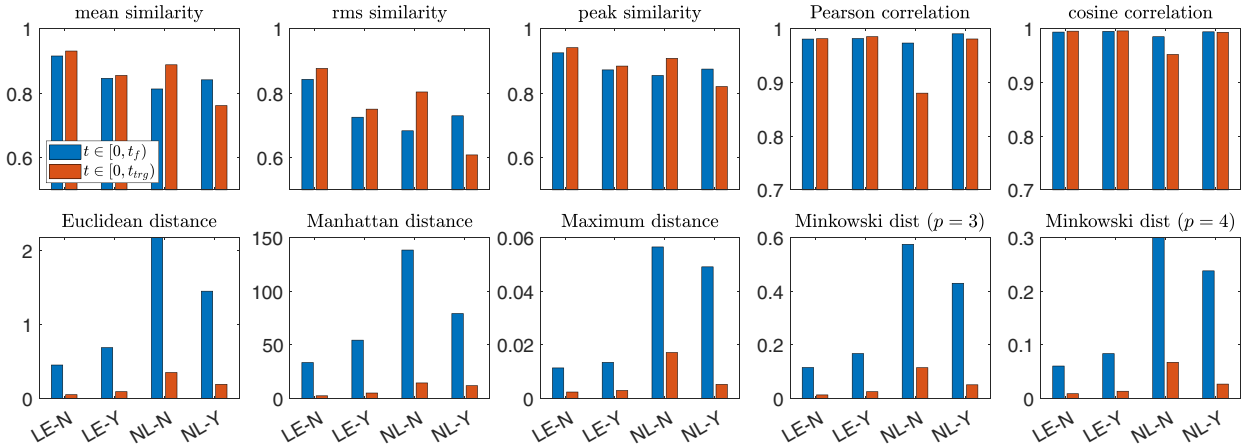



**FIGURE 12** | Quantification of similarity between IAA and IDA curves for crest vertical displacement, and four modeling scenarios. Metrics are provided in two zones: up to target time, and the entire simulation duration. LE: linear elastic, NL: non-linear, N: massless foundation, Y: massed foundation.

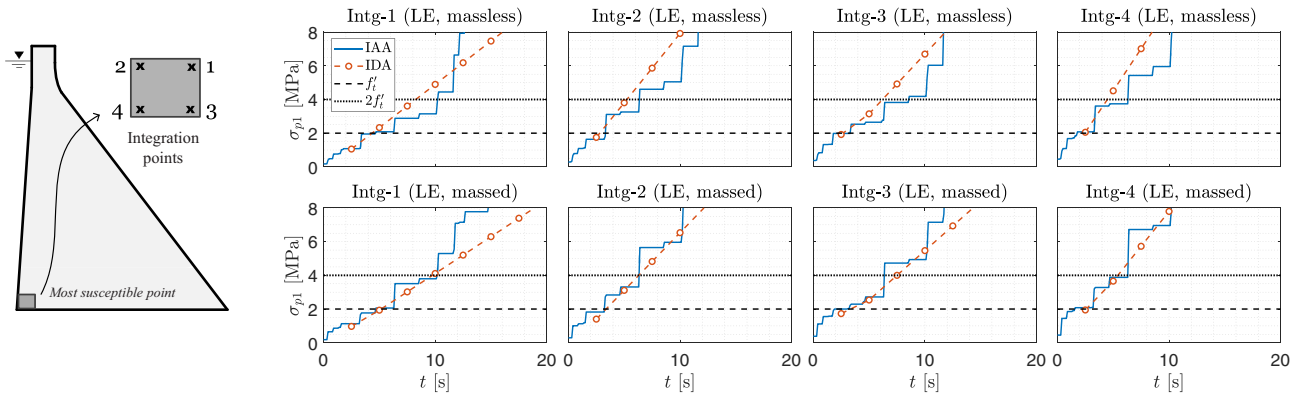



**FIGURE 13** | Comparison of first principal stress at the heel from IAA and IDA for two linear elastic finite element models

its direction. The capacity curves derived from IAA closely align with those from IDA for both foundation modeling approaches, across all four integration points. However, it is essential to recognize the influence of smoothing effects when interpreting these results. The stochastic nature of IAA generation may introduce local fluctuations in stress values; thus, applying a smoothing technique helps in presenting a more consistent and interpretable curve that better reflects the overall trend. Also, it is important to focus on stress ranges within practical engineering limits, particularly $f_t'$ to $2f_t'$ (in this case 2-4 MPa), where the IAA's predictive accuracy is most relevant. In summary, while discrepancies may be observed at stress values significantly exceeding practical design considerations (e.g., five times the tensile strength), the IAA provides a reliable estimation of IDA within the ranges most relevant to engineering analysis and design. Within this critical range, IAA not only demonstrates its capability in estimating global responses but also proves effective in accurately approximating local stress responses.

## 4.5 | Damage Index and Crack Profile

In Section "Principal Stresses", the focus was on comparing stress responses in linear elastic models. On the other hand, for nonlinear models, the comparison can be conducted in terms of the damage index (DI) and crack profile. In dam engineering, various damage indices have been defined [27]. In this paper, the damage index is chosen as the ratio of the damaged area to the total cross-sectional area. This choice is made due to its direct connection with the path of cracks that may form within the structure.

$$DI = \frac{\sum_{i=1}^{N_e} A_i \times d_{t,i}}{A_t} \tag{28}$$

where, $A_i$ is the elemental area, $d_{t,i} \in [0, 1]$ is the extent of the damage in the element, and $A_t$ is the total area. The dam is divided into three regions, and the DI is computed separately in each of them. These three regions are shown in Figure 14, which includes the bottom 20 m (region I), the middle 70 m (region II), and the top 32 m (region III).

Figure 14 illustrates the damage index for various regions within the dam, as well as the DI calculated for the entire structure as a whole. The comparison between IDA and IAA damage indices reveals good agreement in region-I. In region-II, the DIs are closely aligned, exhibiting similar trends. DIs in region-III also show comparable trends, although the IAA curve lacks the



10969845, 0, Downloaded from https://onlinelibrary.wiley.com/doi/10.1002/eqe.70292 by National Institute Of Stds and Technology, Wiley Online Library on [02/11/2026]. See the Terms and Conditions (https://onlinelibrary.wiley.com/terms-and-conditions) on Wiley Online Library for rules of use; OA articles are governed by the applicable Creative Commons License

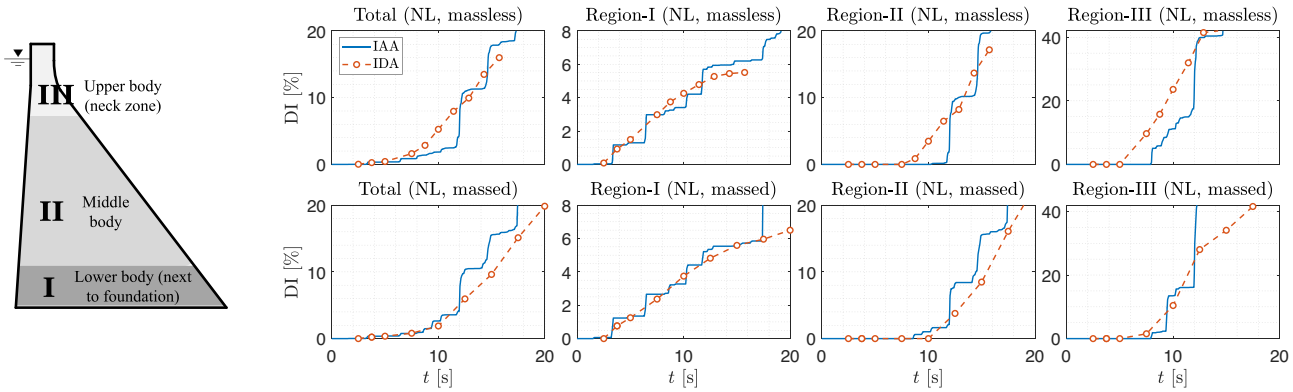
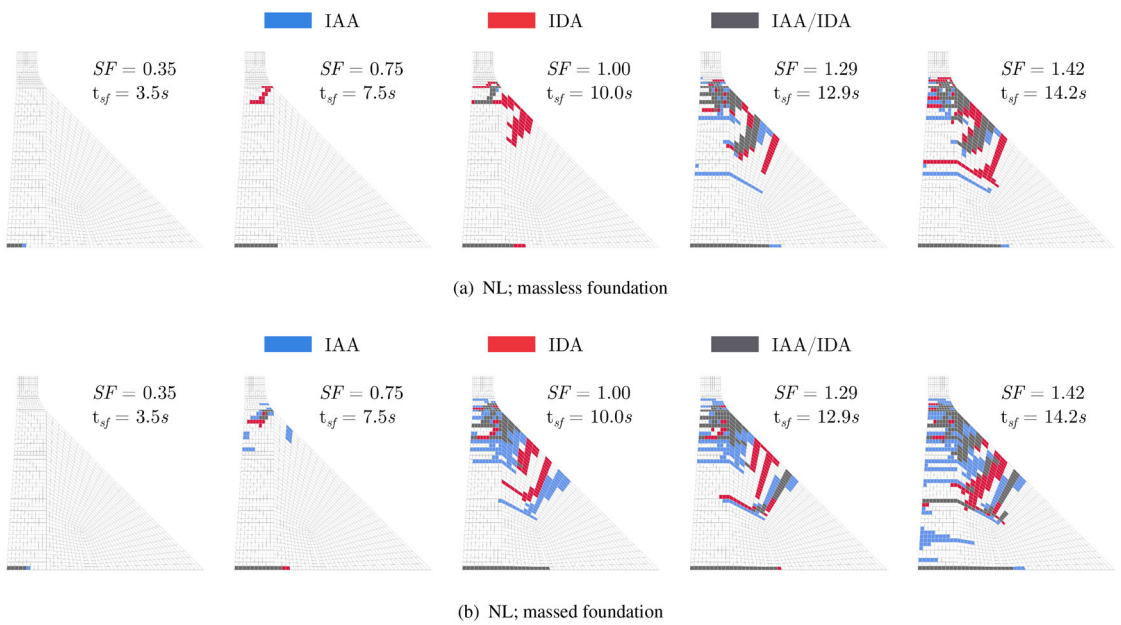



**FIGURE 14** | Comparison of damage index from IAA and IDA for two non-linear finite element models




(a) NL; massless foundation

(b) NL; massed foundation

**FIGURE 15** | Evolution of crack profile for nonlinear models based on IDA and IAA methods. The black color is shared between IDA and IAA, while the blue and red colors only refer to IAA and IDA, respectively.

smoothing present in the IDA curve. This smoothing discrepancy could potentially be improved by converting time to one of the IM parameters discussed in the preceding sections. For the total DI, the massless foundation model shows a higher value for IDA compared to IAA. Conversely, the massed foundation model's total DI closely matches up to a time of $t = 12$ s, corresponding to approximately 30% damage. Beyond this point, IAA displays a rapid rise in the damage index, while the rate of increase in IDA is more gradual.

Figure 15 presents a comparison between the crack patterns of the massless and massed foundation models. In all cases, both IDA and IAA analyses exhibit crack paths originating at the dam's heel and progressing at a closely aligned rate from the upstream face (the natural rocking joint of the dam) toward the downstream face. Subsequently, cracks begin to emerge at the neck and subsequently in the main body (region-II) of the dam. While the crack paths in the massless foundation model demonstrate a strong agreement over time, those in the massed foundation model display a greater degree of dispersion.

For both methods, the crack paths are similar at the beginning and close to the failure point of the analysis. However, the evolution of crack paths differs between the two systems. For some cracks, the path follows a similar trend, although the initiation point slightly differs. Cracks in the IDA approach tend to be more localized, with narrower shapes, whereas those in the IAA method are more widely dispersed. This discrepancy arises from the greater complexity of the massed model, as the massed foundation system acts as a frequency domain filter for the seismic motion. Deconvolution techniques, like the one employed in this study, target specific frequency ranges to achieve good agreement between the target and recorded seismic input. However, such techniques do not guarantee a perfect match of frequency contents across the entire spectrum. Nonetheless, we acknowledge variations between IDA and IAA at higher scale factors, particularly in scenarios approaching or surpassing



10969845, 0, Downloaded from https://onlinelibrary.wiley.com/doi/10.1002/eqe.70292 by National Institute Of Stds and Technology, Wiley Online Library on [02/11/2026]. See the Terms and Conditions (https://onlinelibrary.wiley.com/terms-and-conditions) on Wiley Online Library for rules of use; OA articles are governed by the applicable Creative Commons License

structural collapse, which may be of less consequence in typical engineering applications.

Given the complex nature of the problem and the inherent limitations of deconvolution techniques, differences in crack paths and DIs as observed in this section are reasonable. Moreover, the overall similarities in crack paths, combined with the congruence of DIs and global EDPs, reinforce the notion that IAA holds promise as a technique for seismic analysis of dams.

The reader should be aware that, like all approximate methods, IAA has an optimal application range, beyond which discrepancies may become more pronounced. One such limitation is associated with pulse duration and the effective number of response cycles. The IAAs generated in this paper address this issue indirectly through the inclusion of hysteretic energy compatibility in the optimization process. Since hysteretic energy is cumulative, it reflects the effect of repeated nonlinear response cycles and is more sensitive to excitation duration than peak-only quantities such as spectral acceleration or maximum displacement. Therefore, the present formulation does not attempt to make the IAA a duration-compatible ground motion record in the conventional sense; rather, it attempts to reproduce the duration-sensitive nonlinear response demand through the hysteretic energy term.

However, it is practically challenging to directly align the duration of an IAA with that of a target ground motion, especially when considering the dynamic nature of scale factors used in IDA. For instance, if both the IAA and a target ground motion are assigned a 60-s duration, and IDA applies a scale factor of SF = 0.5 to the ground motion, the comparative IAA response would theoretically correspond to the first 30 s of the IAA if a linear time–scale-factor mapping is used. This adjustment effectively removes half of the acceleration pulses or cycles that would have been present in a full 60-s IAA analysis. Conversely, for SF > 1, the corresponding IAA time may exceed the original target duration unless the IAA is generated for a longer target time. This illustrates a fundamental discrepancy in how IAA time and scaled IDA records are compared. Thus, a strict one-to-one temporal correspondence between IAA and IDA is not generally possible under different scaling conditions.

Two possible extensions can be considered when duration effects are expected to control the response of nonlinear degrading systems. First, the IAA objective function can be augmented by adding explicit duration-sensitive or cumulative ground-motion measures, such as Arias intensity, cumulative absolute velocity, significant duration, or cycle-count-based damage indices. For example, an extended objective function may be written as

$$F_{\text{aug}} = F_{\text{IAA}} + \alpha_{I_A} \int_0^{t_{\max}} \left[I_A(t) - I_A^*(t)\right]^2 \mathrm{d}t + \alpha_{\text{CAV}} \int_0^{t_{\max}} \left[\text{CAV}(t) - \text{CAV}^*(t)\right]^2 \mathrm{d}t + \alpha_D \left[D_{5-95} - D_{5-95}^*\right]^2, \tag{29}$$

where $I_A(t)$ is the cumulative Arias intensity, $\text{CAV}(t)$ is the cumulative absolute velocity, and $D_{5-95}$ is the significant duration. The starred quantities denote the corresponding target values obtained from the reference ground motion, and the $\alpha$ terms are weight factors. Second, the target time $t_{\text{trg}}$ can be increased, for example from 10 s to 15 s or 20 s or longer, when long-duration or cascading-type motions are of interest. This introduces more cycles into the IAA before reaching the response level associated with the unscaled reference ground motion. These extensions are outside the scope of the present study.

## 5 | Conclusions

The accurate seismic risk assessment of critical structures and infrastructure demands the appropriate consideration of uncertainties. Variabilities in ground motions and material properties are primary sources of uncertainty that significantly impact analysis outcomes. Explicitly accounting for these uncertainties in the numerical modeling of complex structures, such as bridges, nuclear power plants, and dams, often requires extensive computational resources that may not be readily available, especially for practical engineering applications.

While the utilization of AI-based proxy models holds promise in reducing the computational demands of seismic risk assessment for complex structures, its widespread adoption remains primarily within research domains. In this context, the emerging technique of Intensifying Artificial Acceleration (IAA) provides an alternative approach to estimate the seismic response of structures in a probabilistic manner, while substantially mitigating the computational burden. Once IAA models are generated, this method becomes viable not only for academic research but also for practical engineering use, given its relatively lower computational costs compared to other probabilistic techniques, and its simplified implementation compared to complex proxy modeling methods.

This study has extended the concept of ground motion-specific IAAs to the realm of multi-component records. The research addresses two primary questions regarding the application of multicomponent, ground motion-specific IAAs: (1) their (limited) validation in comparison to single-record multicomponent IDA, and (2) the impact of different soil-structure modeling assumptions. While the detailed findings have been elaborated in the paper, the following overarching conclusions can be drawn:

Multicomponent, ground motion-specific IAAs demonstrate their efficacy in accurately estimating the seismic response of complex structural systems, such as concrete gravity dams. This conclusion holds true across various modeling scenarios, including different material behaviors (linear and non-linear) and foundation models (massed and massless).

Diverse metrics and multiple IMs have been utilized for direct comparisons between capacity curves obtained from IDA and IAA. Given the utilization of multicomponent accelerations, the agreement in the results remains strong, especially within the time interval $[0, t_{trg}]$.

For linear elastic models, the first principal stress at the dam heel (point A) exhibited a consistent good agreement between IDA and IAA.



10969845, 0, Downloaded from https://onlinelibrary.wiley.com/doi/10.1002/eqe.70292 by National Institute Of Stds and Technology, Wiley Online Library on [02/11/2026]. See the Terms and Conditions (https://onlinelibrary.wiley.com/terms-and-conditions) on Wiley Online Library for rules of use; OA articles are governed by the applicable Creative Commons License

In non-linear models, a comparison of damage indices in three distinct zones of the dam body (top, middle, and bottom), along with the assessment of crack profiles, was conducted. While some discrepancies were observed, especially in crack profiles, they were found to be reasonable given the inherent non-linearity of the problem. The overall localization of damage was comparable between the two analysis techniques, as evidenced by the high agreement in terms of damage index curves.

While this paper provides a detailed comparison between single-record IDA and record-compatible IAAs, the study has several limitations. First, the validation is performed using a particular ground motion record (as a proof of concept study) and one foundation-structure model; therefore, the conclusions should not yet be generalized to all ground motions, or structural systems. Second, the finite element model adopts specific modeling assumptions, including a two-dimensional dam–foundation idealization, linear elastic foundation behavior, and a perfectly bonded dam–foundation interface. Third, the nonlinear SDOF systems used in the IAA calibration are based on bilinear non-degrading hysteretic behavior and therefore do not explicitly capture stiffness degradation, strength deterioration, or pinching effects. Finally, duration effects are considered indirectly through hysteretic energy compatibility. Further research is therefore needed to validate the approach using additional ground motion records, different structural systems, alternative modeling assumptions, and duration-sensitive degrading systems. Future studies should also investigate fragility functions derived from multi-record IDA and corresponding suites of record-compatible IAAs within a full PBEE framework.

### Author Contributions

We, M. Amin Hariri-Ardebili, Giacomo Sevieri, Carlo Resta, Golsa Mahdavi, Anna De Falco, Siamak Sattar, and Sissy Nikolaou, hereby confirm that we are aware of the submission of the paper to the journal Earthquake Engineering and Structural Dynamics. We fully understand the submission requirements and the content of the paper, and we hereby give our consent for the paper to be submitted to EESD for peer review and potential publication.


### Acknowledgment

Certain commercial equipment, instruments, or materials (or suppliers, or software, …) are identified in this paper to foster understanding. Such identification does not imply recommendation or endorsement by the National Institute of Standards and Technology, nor does it imply that the materials or equipment identified are necessarily the best available for the purpose.


### Conflicts of Interest

The authors declare no conflicts of interest.

### Data Availability Statement

The data that support the findings of this study are available from the corresponding author upon reasonable request.

### Endnotes

[1] The notation $t_{trg}$ and $t_{sf}$ are related but not identical. The target time $t_{trg}$ is prescribed during IAA generation and defines the time at which the IAA target quantities correspond to those of the unscaled reference ground motion. In this study, $t_{trg} = 10$ s. The mapping time $t_{sf}$ is used after the IAA is generated to relate an IAA response at time $t_{sf}$ to the response of the reference ground motion scaled by $SF = t_{sf}/t_{trg}$.

### References


1. M. Wieland, "Seismic Hazard and Seismic Design and Safety Aspects of Large Dam Projects," in *Perspectives on European Earthquake Engineering and Seismology* (Springer, 2014), 627–650.

2. M. A. Hariri-Ardebili, R. L. Segura, and J. W. Salamon, *Performance-Based Earthquake Engineering of Concrete Dams* (Springer, 2026).

3. G. Sevieri, A. De Falco, and G. Marmo, "Shedding Light on the Effect of Uncertainties in the Seismic Fragility Analysis of Existing Concrete Dams," *Infrastructures* 5, no. 3 (2020): 22.

4. G. Sevieri and A. De Falco, "Dynamic Structural Health Monitoring for Concrete Gravity Dams Based on the Bayesian Inference," *Journal of Civil Structural Health Monitoring* 10 (2020): 235–250.

5. M. Hariri-Ardebili and V. Saouma, "Random Response Spectrum Analysis of Gravity Dam Classes: Simplified, Practical, and Fast Approach," *Earthquake Spectra* 34, no. 2 (2018): 941–975.

6. USACE, "Earthquake Design and Evaluation of Concrete Hydraulic Structures," EM 1110-2-6053, Department of the Army, U.S. Army Corps of Engineers, Washington D.C., USA (2007).

7. USACE, "Gravity Dam Design," EM 1110-2-2200, Department of the Army, U.S. Army Corps of Engineers, Washington D.C., USA (1995).

8. G. Fenves and A. Chopra, "Simplified Earthquake Analysis of Concrete Gravity Dams: Separate Hydrodynamic and Foundation Interaction Effects," *Journal of Engineering Mechanics* 111, no. 6 (1985): 715–735.

9. G. Fenves and A. Chopra, "Simplified Earthquake Analysis of Concrete Gravity Dams: Combined Hydrodynamic and Foundation Interaction Effects," *Journal of Engineering Mechanics* 111, no. 6 (1985): 736–756.

10. FERC, "Engineering Guidelines for the Evaluation of Hydropower Projects, Chapter 11: Arch dams,", Federal Energy Regulatory Commission, Washington, DC, USA (1999).

11. A. Løkke and A. Chopra, "Direct Finite Element Method for Nonlinear Analysis of Semi-Unbounded Dam–Water–Foundation Rock Systems," *Earthquake Engineering & Structural Dynamics* 46, no. 8 (2017): 1267–1285.

12. D. Vamvatsikos and C. Cornell, "Applied Incremental Dynamic Analysis," *Earthquake Spectra* 20 (2004): 523–553.

13. M. Alembagheri and M. Ghaemian, "Seismic Assessment of Concrete Gravity Dams Using Capacity Estimation and Damage Indexes," *Earthquake Engineering and Structural Dynamics* 42 (2013): 123–144.

14. B. Soysal, B. Binici, and Y. Arici, "Investigation of the Relationship of Seismic Intensity Measures and the Accumulation of Damage on Concrete Gravity Dams Using Incremental Dynamic Analysis," *Earthquake Engineering and Structural Dynamics* 45 (2016): 719–737.

15. M. Hariri-Ardebili and V. Saouma, "Collapse Fragility Curves for Concrete Dams: Comprehensive Study," *ASCE Journal of Structural Engineering* 142, no. 10 (2016): 04016075.

16. R. Segura, C. Bernier, C. Durand, and P. Paultre, "Modelling and Characterizing a Concrete Gravity Dam for Fragility Analysis," *Infrastructures* 4, no. 4 (2019): 62.

17. G. Sevieri, A. De Falco, M. Andreini, and H. G. Matthies, "Hierarchical Bayesian Framework for Uncertainty Reduction in the Seismic Fragility Analysis of Concrete Gravity Dams," *Engineering Structures* 246 (2021): 113001.

18. M. Hariri-Ardebili and V. Saouma, "Probabilistic Seismic Demand Model and Optimal Intensity Measure for Concrete Dams," *Structural Safety* 59 (2016): 67–85.

19. M. Hariri-Ardebili, V. Saouma, and K. Porter, "Quantification of Seismic Potential Failure Modes in Concrete Dams," *Earthquake Engineering and Structural Dynamics* 45 (2016): 979–997.





10969845, 0, Downloaded from https://onlinelibrary.wiley.com/doi/10.1002/eqe.70292 by National Institute Of Stds and Technology, Wiley Online Library on [02/11/2026]. See the Terms and Conditions (https://onlinelibrary.wiley.com/terms-and-conditions) on Wiley Online Library for rules of use; OA articles are governed by the applicable Creative Commons License

20. C. Bernier, R. Monteiro, and P. Paultre, "Using the Conditional Spectrum Method for Improved Fragility Assessment of Concrete Gravity Dams in Eastern Canada," *Earthquake Spectra* 32, no. 3 (2016): 1449–1468.

21. F. Salazar and M. Hariri-Ardebili, "Coupling Machine Learning and Stochastic Finite Element to Evaluate Heterogeneous Concrete Infrastructure," *Engineering Structures* 260 (2022): 114190.

22. F. Salazar and M. Hariri-Ardebili, "Coupling Machine Learning and Stochastic Finite Element to Evaluate Heterogeneous Concrete Infrastructure," *Engineering Structures* 260 (2022): 114190.

23. G. Sevieri, R. Gentile, and C. Galasso, "A Multi-Fidelity Bayesian Framework for Robust Seismic Fragility Analysis," *Earthquake Engineering & Structural Dynamics* 50, no. 15 (2021): 4199–4219.

24. H. E. Estekanchi, M. Mashayekhi, H. Vafai, G. Ahmadi, S. A. Mirfarhadi, and M. Harati, "A State-of-Knowledge Review on the Endurance Time Method," *Structures* 27 (2020): 2288–2299.

25. H. Estekanchi, V. Valamanesh, and A. Vafai, "Application of Endurance Time Method in Linear Seismic Analysis," *Engineering Structures* 29, no. 10 (2007): 2551–2562.

26. H. E. Estekanchi and H. A. Vafai, *Seismic Analysis and Design Using the Endurance Time Method* (CRC Press, 2021).

27. M. Hariri-Ardebili, L. Furgani, M. Meghella, and V. Saouma, "A New Class of Seismic Damage and Performance Indices for Arch Dams via ETA Method," *Engineering Structures* 110 (2016): 145–160.

28. J. Salamon, M. Hariri-Ardebili, H. Estekanchi, and M. Mashayekhi, "Seismic Assessment of a Dam-Foundation-Reservoir System Using Endurance Time Analysis," in *Sustainable and Safe Dams Around the World* (CRC Press, 2019), 2649–2659.

29. Q. Xu, S. Xu, J. Chen, and J. Li, "A Modified Endurance Time Analysis Algorithm to Correct Duration Effects for a Concrete Gravity Dam," *International Journal of Geomechanics* 22, no. 2 (2022): 04021285.

30. J. Ashrafifar and H. Estekanchi, "Life-Cycle Seismic Fragility and Resilience Assessment of Aging Bridges Using the Endurance Time Method," *Soil Dynamics and Earthquake Engineering* 164 (2023): 107524.

31. A. S. Movahhed, A. Shirkhani, S. Zardari, M. Mashayekhi, E. N. Farsangi, and A. Majdi, "Modified Endurance Time Method for Seismic Performance Assessment of Base-Isolated Structures," *Journal of Building Engineering* 67 (2023): 105955.

32. J. Wang, H. Wang, P. Pan, et al., "Endurance Time Analysis for Seismic Performance of Underground Structures Subjected to Mainshock-Aftershock Sequences," *Engineering Structures* 306 (2024): 117879.

33. B. Sun, P. Wang, G. Zhang, M. Deng, W. Liu, and J. Xu, "Endurance Time History Analysis of the Seismic Behavior and Performance Assessment of Hydro-Chemo-Mechanical Degradation-Affected Hydraulic Tunnels With Service Time," *Underground Space* 17 (2024): 207–225.

34. S. Xu, Q. Xu, J. Chen, and J. Li, "Improved Endurance Time Analysis for Seismic Responses of Concrete Dam Under Near-Fault Pulse-Like Ground Motions," *Engineering Structures* 270 (2022): 114912.

35. H. Sun, X. Liu, S. I. Sadat, et al., "Seismic Performance of CFST Piers in Two-Span Continuous Girder Bridge Under Multiple Earthquakes Using Endurance Time Analysis," *Soil Dynamics and Earthquake Engineering* 198 (2025): 109549.

36. M. Mashayekhi, M. Sarcheshmehpour, S. A. Mirfarhadi, and H. E. Estekanchi, "Multidirectional Seismic Assessment of Structures Using Damage-Compatible Endurance Time Intensifying Excitations," *Structures* 88 (2026): 111990.

37. M. Hariri-Ardebili, S. Sattar, and H. Estekanchi, "Performance-Based Seismic Assessment of Steel Frames Using Endurance Time Analysis," *Engineering Structures* 69 (2014): 216–234.

38. M. Hariri-Ardebili and S. Sattar, "Myths and Realities About ETA," *Ocean Engineering* 221 (2021): 108499.

39. American Society of Mechanical Engineers, *Guide for Verification and Validation in Computational Solid Mechanics* (ASME, 2006).

40. J. W. Baker, "Measuring Bias in Structural Response Caused by Ground Motion Scaling," in *8th Pacific Conference on Earthquake Engineering, Singapore* (2007), 1–8.

41. Applied Technology Council, "Quantification of Building Seismic Performance Factors (FEMA P695, ATC-63)," (2009).

42. T. Lin and J. W. Baker, "Introducing Adaptive Incremental Dynamic Analysis: A New Tool for Linking Ground Motion Selection and Structural Response Assessment," in *11th International Conference on Structural Safety and Reliability, New York* (2013), 805–811.

43. M. Kohrangi, D. Vamvatsikos, and P. Bazzurro, "Multi-Level Conditional Spectrum-Based Record Selection for IDA," *Earthquake Spectra* 36, no. 4 (2020): 1976–1994.

44. M. Hariri-Ardebili, G. Sevieri, C. Resta, A. De Falco, S. Nikolaou, and S. Sattar, "Bridging IAA and IDA: A Conceptual Framework, Application, and Implication in Risk Assessment," *International Journal of Disaster Risk Reduction* 116 (2025): 105005.

45. A. Nozari and H. Estekanchi, "Optimization of Endurance Time Acceleration Functions for Seismic Assessment of Structures," *International Journal of Optimization in Civil Engineering* 1 (2011): 257–277.

46. M. Mashayekhi, H. Estekanchi, H. Vafai, and S. A. Mirfarhadi, "Development of Hysteretic Energy Compatible Endurance Time Excitations and Its Application," *Engineering Structures* 177 (2018): 753–769.

47. M. Mashayekhi, H. E. Estekanchi, A. Vafai, and S. A. Mirfarhadi, "Simulation of Cumulative Absolute Velocity Consistent Endurance Time Excitations," *Journal of Earthquake Engineering* 25, no. 5 (2021): 892–917.

48. M. Shinozuka and G. Deodatis, "Simulation of Multi-Dimensional Gaussian Stochastic Fields by Spectral Representation," *Applied Mechanics Reviews* 49, no. 1 (1996): 29–53.

49. D. A. Gasparini and E. H. Vanmarcke, *SIMQKE: A Program for Artificial Motion Generation: User's Manual and Documentation* (Department of Civil Engineering, Massachusetts Institute of Technology, Cambridge, MA, 1976).

50. D. M. Boore, "Stochastic Simulation of High-Frequency Ground Motions Based on Seismological Models of the Radiated Spectra," *Bulletin of the Seismological Society of America* 73, no. 6A (1983): 1865–1894.

51. R. W. Clough and J. Penzien, *Dynamics of Structures* (McGraw-Hill Inc., 1993).

52. S. Rezaeian and A. Der Kiureghian, "Simulation of Synthetic Ground Motions for Specified Earthquake and Site Characteristics," *Earthquake Engineering & Structural Dynamics* 39, no. 10 (2010): 1155–1180.

53. K. Kanai, "Semi-Empirical Formula for the Seismic Characteristics of the Ground," *Bull Earthquake Research Institute* 35 (1957): 309–325.

54. H. Tajimi, "A Statistical Method of Determining the Maximum Response of a Building Structure during an Earthquake," in *Proceedings of the 2nd World Conference on Earthquake Engineering*, 2 (Tokyo and Kyoto, Japan, 1960), 781–798.

55. D. M. Boore, "Simulation of Ground Motion Using the Stochastic Method," *Pure and Applied Geophysics* 160 (2003): 635–676.

56. J. Hancock, J. Watson-Lamprey, N. A. Abrahamson, et al., "An Improved Method of Matching Response Spectra of Recorded Earthquake Ground Motion Using Wavelets," *Journal of Earthquake Engineering* 10, no. spec01 (2006): 67–89.

57. Y. Pang, L. Cai, W. He, and L. Wu, "Seismic Assessment of Deep Water Bridges in Reservoir Considering Hydrodynamic Effects Using Endurance Time Analysis," *Ocean Engineering* 198 (2020): 106846.

58. S. Li, K. Liu, X. Liu, C. Zhai, and F. Xie, "Efficient Structural Seismic Performance Evaluation Method Using Improved Endurance Time Analysis," *Earthquake Engineering and Engineering Vibration* 18, no. 4 (2019): 795–809.

59. R. Zhang, L. Zhang, C. Pan, Q. Chen, and Y. Wang, "Generating High Spectral Consistent Endurance Time Excitations by a Modified



10969845, 0, Downloaded from https://onlinelibrary.wiley.com/doi/10.1002/eqe.70292 by National Institute Of Sids and Technology, Wiley Online Library on [02/11/2026]. See the Terms and Conditions (https://onlinelibrary.wiley.com/terms-and-conditions) on Wiley Online Library for rules of use; OA articles are governed by the applicable Creative Commons License

Time-Domain Spectral Matching Method," *Soil Dynamics and Earthquake Engineering* 145 (2021): 106708.

60. E. Miranda, "Site-Dependent Strength-Reduction Factors," *Journal of Structural Engineering* 119, no. 12 (1993): 3503–3519.

61. J. Salamon, C. Wood, M. Hariri-Ardebili, R. Malm, and G. Faggiani, "Seismic Analysis of Pine Flat Concrete Dam: Formulation and Synthesis of Results," in *ICOLD International Benchmark Workshop on Numerical Analysis of Dams, ICOLD-BW* (Springer, 2019), 3–97.

62. J. J. Moré and D. C. Sorensen, "Computing a Trust Region Step," *SIAM Journal on Scientific and Statistical Computing* 4, no. 3 (1983): 553–572.

63. A. G. Andonov, A. Iliev, and K. S. Apostolov, "Towards Displacement-Based Seismic Assessment of Concrete Dams Using Non-linear Static and Dynamic Procedures," *Structural Engineering International* 23, no. 2 (2013): 132–140.

64. L. Furgani, M. Hariri-Ardebili, M. Meghella, and S. Seyed-Kolbadi, "On the Dynamic Capacity of Concrete Dams," *Infrastructures* 4, no. 3 (2019): 57.

65. K. Porter, "An Overview of PEER's Performance-Based Earthquake Engineering Methodology," in *Proceedings of the Ninth International Conference on Applications of Statistics and Probability in Civil Engineering (ICASP9)* (San Francisco, CA: Civil Engineering Risk and Reliability Association (CERRA), 2003), 1–8.

66. J. Baker, "Efficient Analytical Fragility Function Fitting Using Dynamic Structural Analysis," *Earthquake Spectra* 31, no. 1 (2015): 579–599.

67. J. Salamon, "Evaluation of Numerical Models and Input Parameters in the Analysis of Concrete Dams," DSO-19-13, U.S. Bureau of Reclamation, Denver, Colorado (2018).

68. M. Hariri-Ardebili, "Quantifying Modeling Uncertainties in Seismic Analysis of Dams: Insights From an International Benchmark Study," *Earthquake Engineering & Structural Dynamics* (2024).

69. G. Bolzon, D. Sterpi, G. Mazzà, and A. Frigerio, *Numerical Analysis of Dams: Proceedings of the 15th ICOLD International Benchmark Workshop*, vol. 91 (Springer Nature, 2020).

70. D. Rea, C. Liaw, and A. Chopra, "Dynamic Properties of Pine Flat Dam,", CALIFORNIA UNIV BERKELEY EARTHQUAKE ENGINEERING RESEARCH CENTER (1972).

71. A. Chopra, P. Chakrabarti, and S. Gupta, "Earthquake Response of Concrete Gravity Dams Including Hydrodynamic and Foundation Interaction Effects,", CALIFORNIA UNIV BERKELEY EARTHQUAKE ENGINEERING RESEARCH CENTER (1980).

72. J. W. Chavez and G. Fenves, "Earthquake Response of Concrete Gravity Dams Including Base Sliding," *Journal of Structural Engineering* 121, no. 5 (1995): 865–875.

73. G. Fenves and A. Chopra, "Simplified Analysis for Earthquake Resistant Design of Concrete Gravity Dams," UCB/EERC-85/10, Earthquake Engineering Research Center, Berkeley, CA (1986).

74. ABAQUS, ABAQUS Version 6.14 - Documentation Manual (2014).

75. B. K. Patra, R. Segura, and A. Bagchi, "Modeling Variability in Seismic Analysis of Concrete Gravity Dams: A Parametric Analysis of Koyna and Pine Flat Dams," *Infrastructures* 9, no. 1 (2024): 10.

76. A. De Falco, M. Mori, and G. Sevieri, "Simplified Soil-Structure Interaction Models for Concrete Gravity Dams," in *Proceedings of the 6th European Conference on Computational Mechanics (ECCM 6) and the 7th European Conference on Computational Fluid Dynamics (ECFD 7)* (2018), 2269–2280.

77. V. Saouma, F. Miura, G. Lebon, and Y. Yagome, "A Simplified 3D Model for Soil-Structure Interaction With Radiation Damping and Free Field Input," *Bulletin of Earthquake Engineering* 9 (2011): 1387–1402.

78. E. Wilson, *Three-Dimensional Static and Dynamic Analysis of Structures: A Physical Approach With Emphasis on Earthquake Engineering* (Berkeley, California: Computers and Structures Inc., 2002).

79. J. Wolf, *Dynamic Soil Structure Interaction* (Englewood Cliffs, New Jersey: Prentice-Hall, 1985).

80. J. Lysmer and R. Kuhlemeyer, "Finite Dynamic Model for Infinite Media," *Journal of the Engineering Mechanics Division* 95, no. 4 (1969): 859–878.

81. M. Hariri-Ardebili and H. Mirzabozorg, "A Comparative Study of Seismic Stability of Coupled Arch Dam-Foundation-Reservoir Systems Using Infinite Elements and Viscous Boundary Models," *International Journal of Structural Stability and Dynamics* 13, no. 06 (2013): 1350032.

82. M. Poul and A. Zerva, "Efficient Time-Domain Deconvolution of Seismic Ground Motions Using the Equivalent-Linear Method for Soil-Structure Interaction Analyses," *Soil Dynamics and Earthquake Engineering* 112 (2018): 138–151.

83. J. Lee and G. Fenves, "Plastic-Damage Model for Cyclic Loading of Concrete Structures," *Journal of Engineering Mechanics* 124, no. 8 (1998): 892–900.

84. O. Omidi, S. Valliappan, and V. Lotfi, "Seismic Cracking of Concrete Gravity Dams by Plastic-Damage Model Using Different Damping Mechanisms," *Finite Elements in Analysis and Design* 63 (2013): 80–97.

85. D. Vamvatsikos and C. Cornell, "Incremental Dynamic Analysis," *Earthquake Engineering and Structural Dynamics* 31 (2002): 491–514.

86. C. Cassisi, P. Montalto, M. Aliotta, A. Cannata, and A. Pulvirenti, "Similarity Measures and Dimensionality Reduction Techniques for Time Series Data Mining," in *Advances in Data Mining Knowledge Discovery and Applications* (2012), 71–96.

87. P. Tothong and N. Luco, "Probabilistic Seismic Demand Analysis Using Advanced Ground Motion Intensity Measures," *Earthquake Engineering and Structural Dynamics* 36 (2007): 1837–1860.

88. A. Kostinakis, A. Athanatopoulou, and K. Morfidis, "Correlation Between Ground Motion Intensity Measures and Seismic Damage of 3D R/C Buildings," *Engineering Structures* 82 (2015): 151–167.

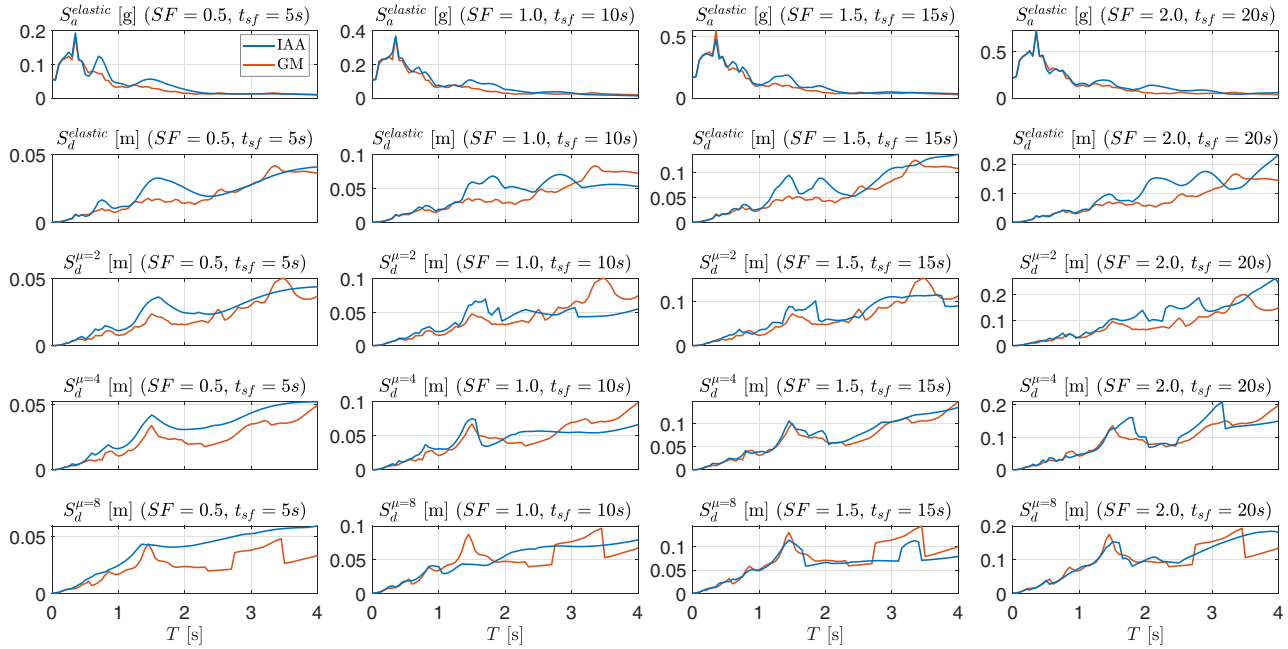
89. Y. Ghanaat, "Failure Modes Approach to Safety Evaluation of Dams," in *Proceedings of the 13th World Conference on Earthquake Engineering* (Vancouver, BC, Canada, 2004).



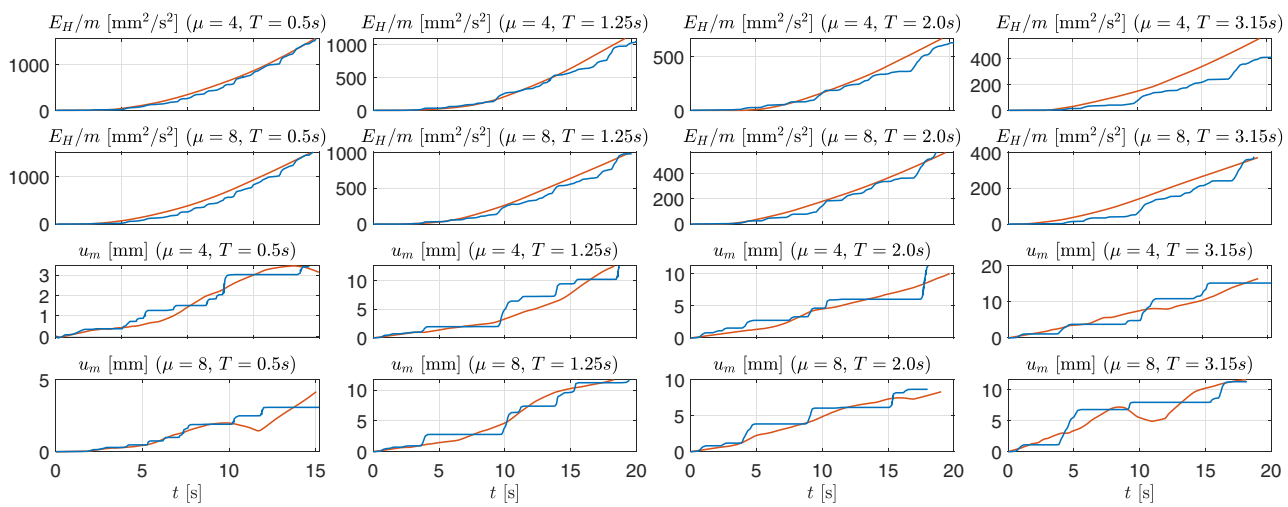
10969845, 0, Downloaded from https://onlinelibrary.wiley.com/doi/10.1002/eqe.70292 by National Institute Of Sids and Technology, Wiley Online Library on [02/11/2026]. See the Terms and Conditions (https://onlinelibrary.wiley.com/terms-and-conditions) on Wiley Online Library for rules of use; OA articles are governed by the applicable Creative Commons License

## Appendix A

See Figures A1 and A2.




(a) Frequency-dependent comparison

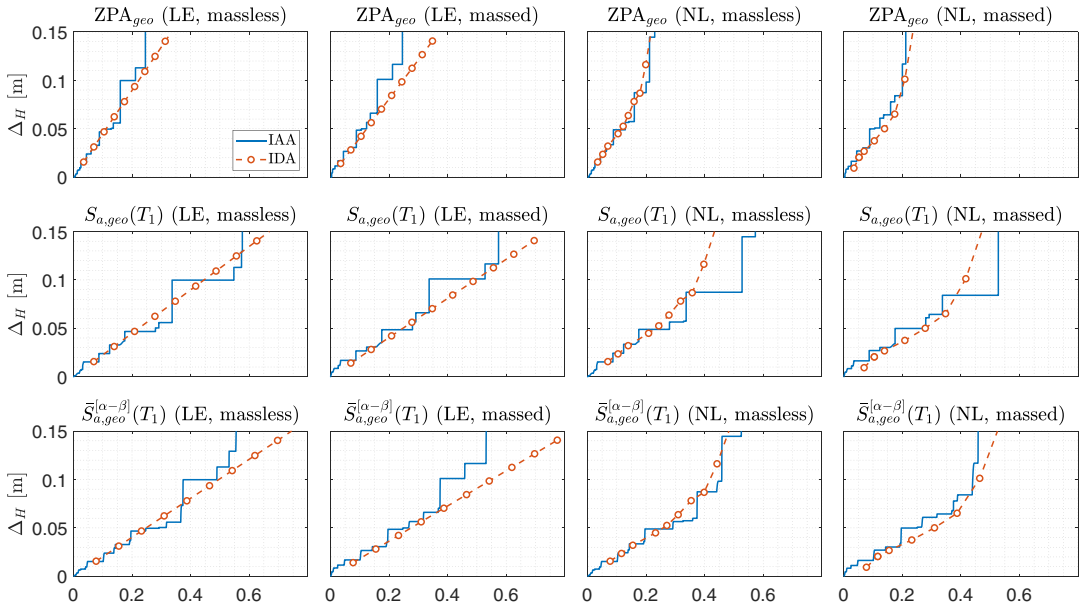



(b) Time-dependent comparison

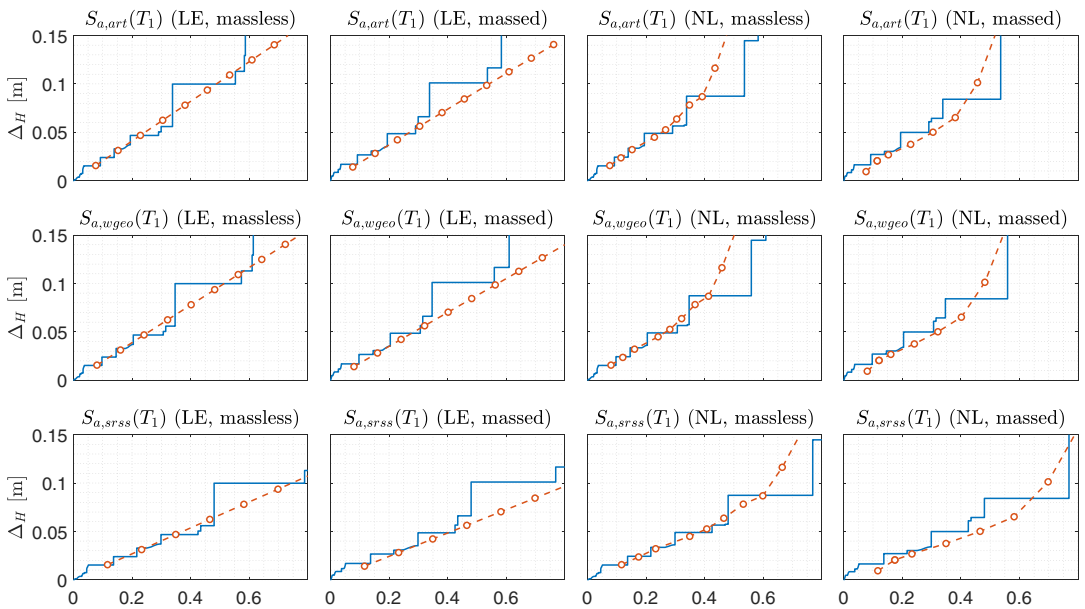
**FIGURE A1** | Comparison of elastic acceleration, elastic / inelastic displacement spectra, nonlinear displacement, and hysteretic energy from target ground motion and the optimized IAA for the vertical component.



10969845, 0, Downloaded from https://onlinelibrary.wiley.com/doi/10.1002/eqe.70292 by National Institute Of Sids and Technology, Wiley Online Library on [02/11/2026]. See the Terms and Conditions (https://onlinelibrary.wiley.com/terms-and-conditions) on Wiley Online Library for rules of use; OA articles are governed by the applicable Creative Commons License




(a) Combining H and V components of various IM using geometric mean method




(b) Combining H and V components of $S_a(T_1)$ using various techniques

**FIGURE A2** | Direct comparison of IAA and IDA in terms of various combined (horizontal and vertical) IM parameters and a global EDP (i.e., horizontal displacement).



10969845, 0, Downloaded from https://onlinelibrary.wiley.com/doi/10.1002/eqe.70292 by National Institute Of Stds and Technology, Wiley Online Library on [02/11/2026]. See the Terms and Conditions (https://onlinelibrary.wiley.com/terms-and-conditions) on Wiley Online Library for rules of use; OA articles are governed by the applicable Creative Commons License